Materials & Design 227 (2023) 111757

Contents lists available at ScienceDirect

Materials & Design

journal homepage: www.elsevier.com/locate/matdes

Towards material and process agnostic features for the classification of pore types in metal additive manufacturing

Mathieu Vandecasteele [a,*], Rob Heylen [b], Domenico Iuso [c], Aditi Thanki [d,e], Wilfried Philips [a], Ann Witvrouw [d,e], Dries Verhees [b], Brian G. Booth [a]

[a] TELIN-IPI, Ghent University – imec, St-Pietersnieuwstraat 41, Gent B-9000, Belgium
[b] Flanders MAKE, Oude Diestersebaan 133, Lommel B-3920, Belgium
[c] imec-Vision Lab, University of Antwerp, Universiteitsplein 1, Antwerpen B-2610, Belgium
[d] MaPS - Department of Mechanical Engineering, KU Leuven, Celestijnenlaan 300B, Leuven B-3001, Belgium
[e] Flanders Make @ KU Leuven, Leuven B-3001, Belgium

HIGHLIGHTS

- An effective strategy for pore type classification in X-ray tomography is presented.
- Pore geometry was studied across three materials and various printer settings.
- Relative measurements of pore geometry generalize better than absolute measures.
- The proposed features enable a general-purpose classifier across print scenarios.

GRAPHICAL ABSTRACT

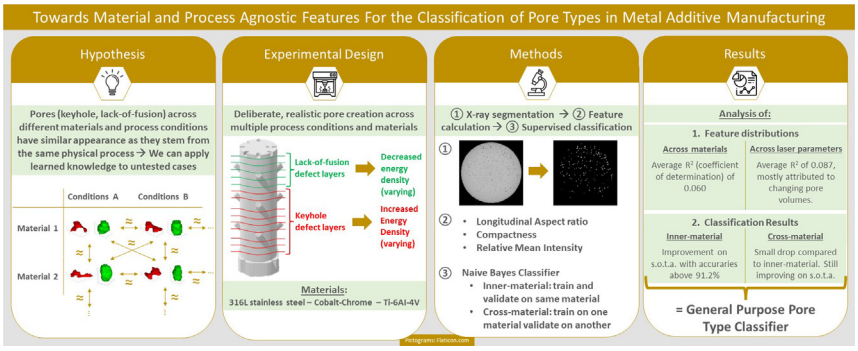

ARTICLE INFO

Article history:
Received 23 September 2022
Revised 26 January 2023
Accepted 15 February 2023
Available online 21 February 2023

Keywords:
Metal additive manufacturing
Powder-bed fusion
Porosity
Pore classification
X-ray tomography

ABSTRACT

The manufacturing of metal parts via powder-bed fusion is often still facing quality issues due to microstructural porosity. Minimizing this porosity remains a priority and requires the optimization of printing process parameters. While the analysis of printed parts using X-ray computed tomography can localize and identify the pore types (e.g. keyhole or lack-of-fusion pores), these pore types can be difficult to identify across printer settings and print materials. Therefore, there is a need for a material and process agnostic approach. This work presents such an approach by considering a set of geometric pore features that do not differ considerably across print scenarios. These features are then leveraged for supervised pore type classification. The distributions of pore features were analyzed in different materials and under varying laser parameters, showing that they behave in a generic way. For classification, it is observed that they outperform other features leveraged in the state-of-the-art for pore classification in a single material, reaching up to 93.0% accuracy. Additionally, accuracies up to 90.2% for cross-material classification were observed by training on pores of one material and validating on another. These results pave the way to a general-purpose pore classification method usable across materials and process conditions.

* Corresponding author.
E-mail address: mathieu.vandecasteele@ugent.be (M. Vandecasteele).

https://doi.org/10.1016/j.matdes.2023.111757
0264-1275/

1. Introduction

The additive Manufacturing (AM), i.e. 3D printing, of metal parts has the potential to revolutionize the manufacturing industry as it offers three key advantages over traditional part manufacturing. First, AM only uses as much material as needed, leading to less material waste as compared to subtractive manufacturing [1]. Second, AM has decreased manufacturing cost and time since no part-specific tools are needed [2]. Third, AM allows an increase of part complexity without an increase of cost [3]. These advantages allow AM to create complex and customized parts at a lower cost than traditional manufacturing.

The laser powder-bed fusion (LPBF) process is a popular technique used in metal AM. During the process, powder particles are deposited and melted by a laser in a layer-wise manner to build up the part. Due to the complexity of this process, a variety of defects may occur in the finished parts. Porosity, or voids in the printed part, remains one of the most challenging defects. Porosity is a result of micro-structural defects, often referred to as pores, that have a negative influence on its strength and mechanical properties [4].

The most commonly-observed pores types are keyhole and lack-of-fusion pores. They are associated with either transferring too much energy into the powder-bed or not transferring enough energy into the powder-bed, respectively. The energy density that is transferred into the powder-bed is partly determined by the laser power and speed. In fact, we can outline a couple of zones in a parameter space spanned by the laser power and speed [5], as seen on Fig. 1a. In Zone I, the parameters are optimal and no porosity is expected to be generated. Zone II is the lack-of-fusion zone, where the energy density is too low to fuse the metal powder, resulting in lack-of-fusion pores. Zone III, the keyhole zone, is associated with an energy density that is too high, resulting in keyhole pores. Finally, zone IV is associated with the phenomenon called balling. In this zone, the melted metal can solidify into isolated spheres. Example X-ray CT slices of keyhole and lack-of-fusion pores can be seen on Fig. 1b and c, while the balling effect can be observed on Fig. 1d. Most of the different sources of porosity

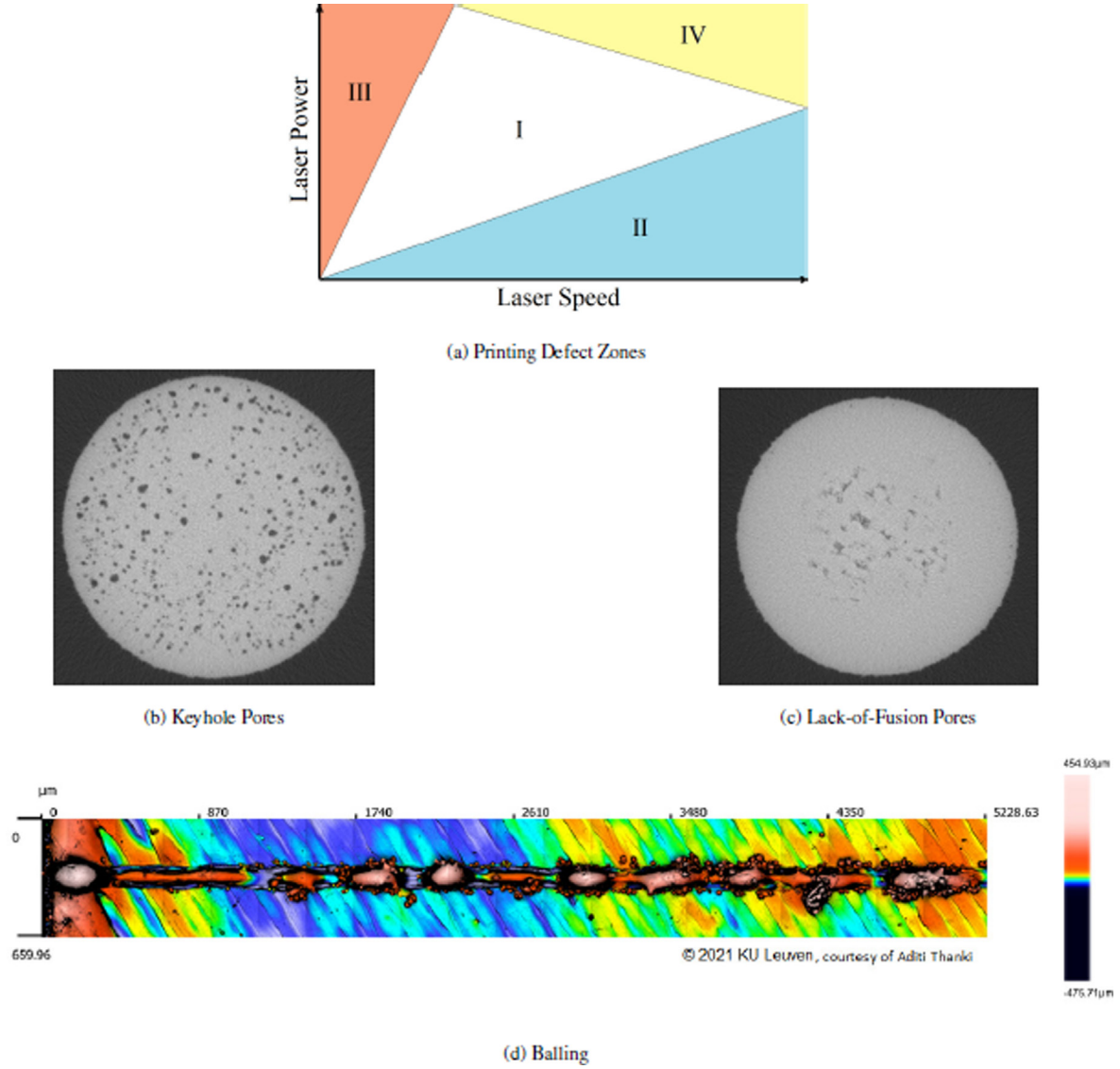

Fig. 1. Overview of 3D printing defects. **(a)** The different zones influenced by laser speed and power. Zone I is optimal and may produce high quality parts. Zone II produces lack-of-fusion porosity, zone III produces keyhole porosity and zone IV produces defects due to a phenomenon called balling. **(b)** An example X-ray CT slice of a layer where keyhole porosity is observed. These pores were created due to the process operating in zone III. **(c)** An example X-ray CT slice of a layer where lack-of-fusion porosity is observed. These pores were created due to the process operating in zone II. **(d)** A 2.5D surface measurement, using confocal microscopy, of a sample where balling can be observed. These defects were created due to the process operating in zone IV.

come down to the fact that there is either too much (keyhole) or not enough energy (lack-of-fusion).

These lack of fusion and keyhole pores can occur due to several reasons, and mitigating all these sources of porosity remains challenging. Porosity can be powder-induced, dependent on the quality of the powder and out of the control of the part manufacturer. Porosity can also be model-induced, where printing parameters for special geometries (e.g. overhangs) have yet to be fully optimized [6]. Stochastic, process-induced variability can also produce porosity due to all kinds of phenomena, such as: melt pool spatter [7,8], heat accumulation [9,10] and plume formation [11,8]. While optimal printing parameters have been estimated for many metals [12–15] and, occasionally for different object geometries [16,17], these printing parameters are, in general, not perfect. These variable printing conditions (e.g. humidity, part geometry) have the effect of locally shifting the boundaries of the defect zones in Fig. 1a, constantly changing which process parameters are optimal. As a result, dependent on part complexity, up to 40% of 3D printed metal objects fail to meet quality standards and need to be scrapped [18]. These challenges are further evidenced by ongoing research on different mitigation strategies such as: post-process heat treatments [19–21], in situ process monitoring systems [22–25] and process optimization by post-process analysis [26–28]. This work will mostly be focused on the last strategy.

The aim of post-process analysis is not only to identify the pores in a part, but is also to find the causes of these pores, i.e. what physical process caused the pore creation [29]. X-ray computed tomography has been shown to provide information on the location, distribution, size, and morphology of pores in a 3D printed part without destroying it [30]. This pore information is useful to narrow down the cause of the porosity, allowing an operator to adjust the printing process to mitigate the creation of these pores. Adjusting the printing process can be interpreted in a broad sense: it may involve changing the build chamber conditions, changing the scanning strategy, adjusting the laser parameters, etc. Regardless of the adjustment employed, the result of these adjustments must be different for keyhole and lack-of-fusion pores. In the former case, the energy density deposited by the laser must decrease, with for the latter, the energy density must increase. As a result of this difference, it is crucial that a pore's type be properly identified.

Keyhole and lack-of-fusion pores have distinct shapes [31]. The dissimilarities in pore shape can be expressed by some morphological features, such as size, surface area, aspect ratio, sphericity etc. The differences in these features between pore types have been investigated in several studies [32–39]. A common classification approach is setting defined limits on some of these features [40–42]. However this can be challenging to apply due to possible overlaps in the range of values of the features between pore types. More elaborate statistical methods have also been proposed to address this problem, such as k-means clustering [41], decision trees and artificial neural networks [43]. Using user defined features can also be completely omitted if using deep neural networks as demonstrated in [44].

While some of the previously mentioned works on pore classification show excellent performance, their evaluation is lacking on two important aspects: robustness to changing process conditions and generalization to other materials. The former is important because a pore's shape is influenced by the extent to which the process conditions deviate from the optimal conditions. For example, typically keyhole pores tend to be become larger as the deviation from the optimal printing conditions increase [45–47]. It is thus essential to investigate if the chosen parameters and methods are robust to these changes to ensure that they are applicable to a wide range of process conditions. The latter aspect is also important because different materials have different thermal conductivities and laser absorptivities, both of which can impact pore shape [48]. By not considering these aspects of pore classification, existing studies provide little information on whether their results can generalize to different printing scenarios and, potentially, to new printing materials. Therefore, the open question remains: could a classification model trained on pores of one material be leveraged on a new material with similar accuracy? To the best of our knowledge, no other study has addressed this question.

Even though pore shapes may vary across process conditions and materials, they still share some underlying similarities because the physics of pore creation is rather consistent across different metals and printing modes (e.g. conduction mode, keyhole mode) [49,50]. The challenge is to find morphological features of pores that show minimal variance across these scenarios. If such features exist, a general purpose pore type classifier could then be created that is usable across materials and process conditions and thus completely process- and material-agnostic. Such a classifier would allow us to leverage our knowledge of pores created under any process condition from any material and apply it to unseen cases.

We hypothesize that there must exist some pore features that show minimal variance across process conditions and materials. Under this hypothesis, it should also be possible to design a general purpose pore type classifier. In this study, we evaluate this hypothesis and, in turn, introduce the following contributions to the field:

- We present geometrical features of pores that show small enough variance across metals and process conditions to allow for generalizability,
- We present a supervised pore type classification method, showing state-of-the-art classification accuracies both within a single material and across materials,
- We evaluate both of these contributions to show that indeed, there is evidence to support the hypothesis that a general purpose classifier is possible.

2. Materials

To test the material-agnostic properties of pore classification, test objects were 3D printed in three different materials: 316L stainless steel, a cobalt-chrome alloy and Ti6AI4V titanium. While these materials were chosen based on their availability, they are common materials in metal AM and make representative test materials. To create porosity, non-optimal energy densities were induced into the power-bed by altering of the laser parameters. The strategy used for altering the laser parameters is explained in more detail in the experimental design section. The specific laser parameters used in the experiments are listed in appendix B. The remaining process parameters are kept at their known optimal levels and are included in the descriptions below.

The steel sample was fabricated using a 3DX DMP320 laser powder bed fusion (LPBF) machine. The laser source of the LPBF machine was an Ytterbium fiber with wavelength of 1064 nm and had a spot size of 75 μm. The print was carried out under an argon atmosphere. The powder particle size of the stainless steel ranged between 20–50 μm. Each layer of the printed part was 30 μm thick and a hatching distance of 100 μm was used.

The Cobalt-chrome sample was printed on a Renishaw machine AM250. The LPBF machine equipped with a pulsed laser operating at wavelength of 1070 nm. The sample was created with particle size of 15–45 μm. The print was executed with layer thickness of 40 μm and single line hatching pattern.

The Ti6AI4V sample was fabricated with an SLM 125 HL machine equipped with a Materialise Control Platform (MCP). The machine employs a ytterbium fiber laser operating at a wavelength of 1080 nm. Printing was carried out under an argon atmosphere. The powder particle sizes range between 15 and 45 μm. Each layer is 30 μm thick and a hatching distance of 130 μm was used.

To identify porosity, the three printed samples were scanned with the UAntwerp FleXCT scanner [51]. For each sample, the source-to-detector distance was set to 650 mm and the source-to-object distance to 43.33 mm. In order to increase the similarity in image quality despite the samples being of different materials, some of the scanner parameters were set specifically for each sample. The steel sample was scanned at 230 kV, with an exposure time of 600 ms, current of 90 μA and copper filtration of 1.5 mm, for a total of 4282 X-ray projections. The cobalt-chrome sample was scanned at 220 kV, exposure time of 1095 ms, current of 75 μA and copper filtration of 1 mm, for 4282 X-ray projections. The titanium sample was scanned at 200 kV, exposure time of 2100 ms, current of 75 μA and copper filtration of 1 mm, for 1443 X-ray projections. Using the FDK reconstruction and a beam-hardening compensation algorithm, 3D X-ray CT images were obtained with a resolution of 10 μm in the three directions. These X-ray CT images provided ground truth information on the porosity of the printed samples.

3. Methods

3.1. Overview

Given a X-ray CT scan of a printed part, our goal is to identify and classify the pores into keyhole and lack-of-fusion classes. The general workflow is outlined in the following subsections. At first the pores are segmented from the bulk material using classical image processing techniques as described in the segmentation subsection. The features for each pore are then calculated as explained in the feature detection subsection. We also justify there why we use the particular features we chose. The feature values for every pore are then input into a trained classification model that determines the pore type. This is outlined in the last subsection. Note that the novelty of this work is situated in the proposed features and the investigation of their material agnosticism and robustness to varying printing parameters. Therefore, the segmentation and classification methods have been deliberately chosen to be standard approaches in order to show that the features do not depend on any bespoke segmentation or classification techniques.

3.2. Segmentation

For the segmentation of pores from the X-ray CT data, we employed the established algorithm of Kim et al. [52] which has previously been validated and has seen widespread use [53–58]. The method is described in pseudo-code in Algorithm 1. For every slice, a denoising is applied by a non-local means filtering with a fixed estimate on the standard deviation of the Gaussian noise. Fig. 2b ($S_{denoised}$ in Algorithm 1) shows an example of a denoised slice from the original slice in Fig. 2a. To segment the pores, Bersen's Local Thresholding algorithm [59] is used with a window size of 5 and a fixed value for the contrast threshold. The result is a binary image where pores are segmented for every slice. If a pore is larger than the window size of Bersen's, the center pixels of the pore may be incorrectly assigned as not being part of the pore. Therefore, after Bersen's thresholding, a hole filling method is applied to close these holes. Fig. 2c ($S_{binaryfill}$ in Algorithm 1) shows the output after this segmentation. Finally, as seen on Fig. 2d ($S_{binarydenoised}$ in Algorithm 1), a median filtering is applied with window size 5 to eliminate very small pores due to partial voluming effects. These artifacts are most notable along the edges of the sample.

To acquire and label individual 3D pores, the binary segmented images are then stacked and a 3D connected components procedure [60] is performed. Finally, and in addition to the work of Kim et al. [52], a marker-based watersheds segmentation [61] was performed on the distance transformation of each individual pore. This was done to correctly separate individual pores that touch each other.

Algorithm 1 Pore Segmentation Algorithm

Input: $Slices = CT\ Scan\ Slices\,(16-bit)$
Output: *Pores*
$BinarySlices \leftarrow \{\}$
for every Slice S **in** Slices **do**
  $S_{denoised} \leftarrow Nonlocalmeans(S_{median}, std = 2000)$
  $S_{binary} \leftarrow Bernsen(S_{denoised}, size = 5, c = 3000)$
  $S_{binaryfill} \leftarrow Fillholes(S_{binary})$
  $S_{binarydenoised} \leftarrow Medianfilter(S_{binaryfill}, size = 5)$
  $BinarySlices.append(S_{binarydenoised})$
end for
$ST \leftarrow Stack(BinarySlices)$
$CC \leftarrow Connectedcomponents3D(ST)$
$Pores \leftarrow \{\}$
for every Component C **in** CC **do**
  $D \leftarrow DistanceTransform(C)$
  $W \leftarrow Watersheds3D(D)$
  for every Pore P **in** W **do**
    $Pores.append(P)$
  end for
end for

Prior to running the experiments, the accuracy of the pore segmentation algorithm was evaluated through a comparison with microscopy imaging. This comparison study is provided in Appendix A and its results visually agree with previously-reported high accuracies [52].

3.3. Feature detection

If the laser energy density supplied to the powder bed is too high, the LPBF process will operate in the keyhole melting mode. In the keyhole regime, the increased laser and vapor pressure creates a deep depression in the meltpool, which can lead to a runaway, tunnel-shaped depression that leaves pores at the bottom [62]. The pores that are created are then contracted into a spherical shape to minimize surface area [63] and are filled with inert gas from the build chamber. Keyhole pores are also more likely to be elongated along the build direction [41]. These physical characteristics can be translated into measurable 3D features and used for classification.

Meanwhile, lack-of-fusion porosity occurs when the supplied energy density is too low. They are created due to an insufficient overlap of successive melt pools [50]. These kind of pores are elongated along the scan direction and may contain unmelted powder particles [64]. Their shape is also rather irregular [65]. Again, these physical characteristics of lack-of-fusion pores can be translated into 3D features.

The spherical nature of keyhole pores, and the irregular nature of lack-of-fusion pores, can be captured in a compactness feature. The compactness of a pore is defined as the ratio of the volume of the pore to the volume of the equivalent sphere with the same radius as the pore:

$$C = \frac{V_{pore}}{\frac{4}{3}\pi R_{pore}^3}. \tag{1}$$

The radius of the pore is defined as being the half of the width of the pore, where the width is the longest linear distance found in the build (XY) plane: $R_{pore} = 1/2 \max(\mathbf{D}_{xy})$. $\mathbf{D}_{xy}$ denotes a vector of all

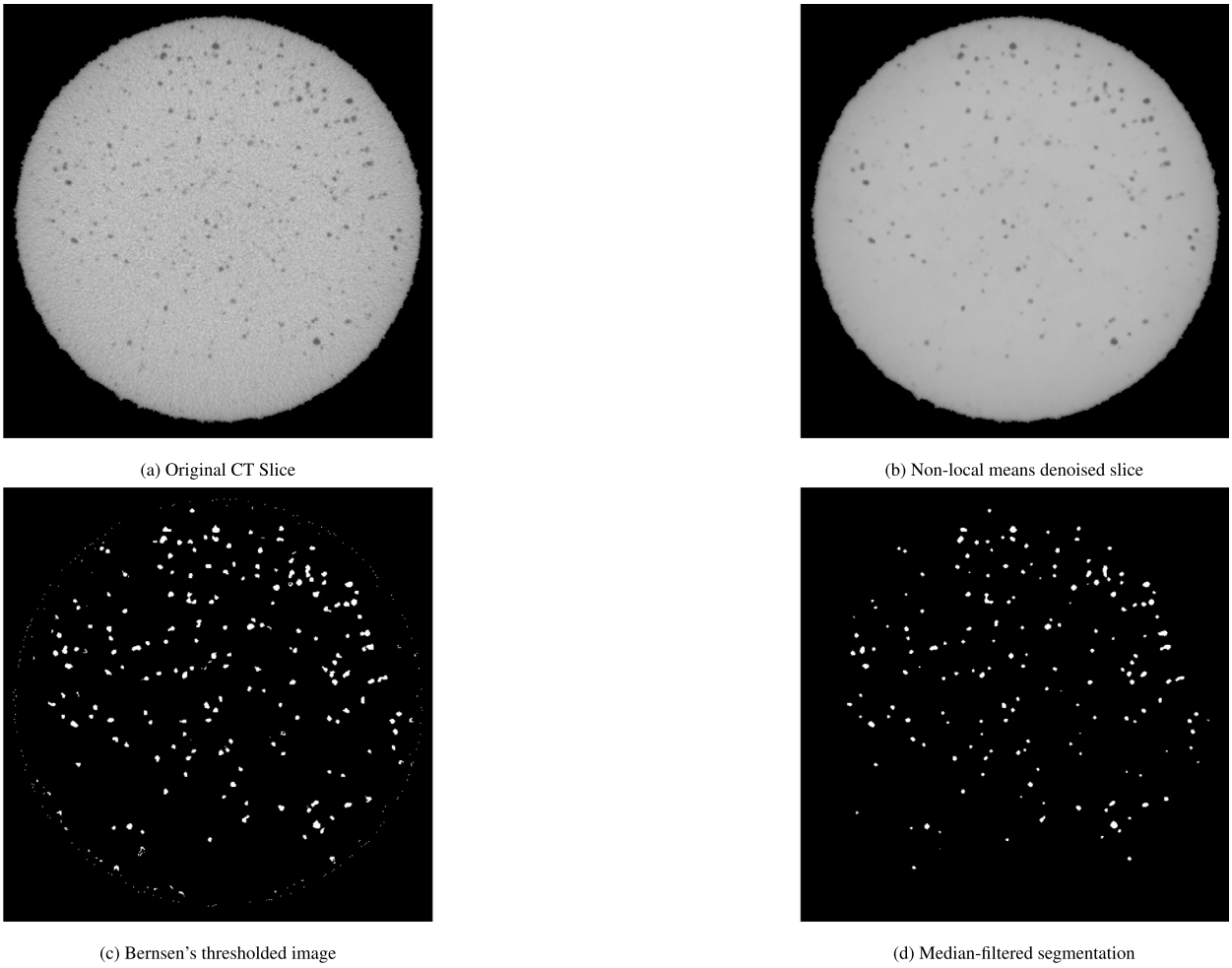

(a) Original CT Slice

(b) Non-local means denoised slice

(c) Bernsen's thresholded image

(d) Median-filtered segmentation

Fig. 2. Intermediate results of applying the segmentation algorithm on an example slice. **(a)** The original unaltered slice. **(b)** Denoising of the slice using non-local means filtering. **(c)** Binarized image by applying Bernsen's local thresholding and hole filling procedure. **(d)** The final binarized image after denoising using a median filter.

pairwise in-plane distances between voxels in the given pore. The compactness feature values for keyhole pores are close to 1 due to their surface area minimization. Meanwhile, lack-of-fusion pores have a more irregular shape, leading to a lower compactness value.

A second feature that we propose is the relative mean intensity. This feature leverages the fact that lack-of-fusion pores may contain unmelted particles. It is defined as the ratio of the mean intensity of the pore's neighborhood to the mean intensity of the pore itself:

$$\widehat{I}_{rel} = \widehat{I}_n / \widehat{I}_p = \left[\sum_{n \in N} I_n\right] / |N| \Big/ \left[\sum_{p \in P} I_p\right] / |P|, \tag{2}$$

with N being the set of all voxels that are part of the pore's *neighborhood*, and $|N|$ being the size of this set. Likewise, P is the set of all voxels that are part of the pore. For lack-of-fusion pores, this feature value is closer to 1 due to the presence of the unmelted powder particles. For keyhole pores, these values are higher as they are filled with whatever gas is present in the build chamber (e.g. argon). It could be argued that the same information may be conveyed by simply using the mean intensity of the pore itself as a feature. However, the intensity of a sample as measured by a X-ray CT system is dependent on the material. By comparing the intensity of a pore to the intensity of the material, the feature is independent of the particular material used.

In order to calculate this relative mean intensity feature, the neighborhood of a pore N has to be properly defined. We define this neighbourhood as the union of all voxels that are within 10 voxels (100 μm) from the pore boundary, minus the voxels of the pore itself and minus the voxels that are part of any other nearby pore. To determine this neighborhood for every pore, a distance transformation map is first computed for the entire binarized volume. This distance transform computes the Euclidean distance of each voxel to the nearest pore. By thresholding the distance transform map and cropping it to include only distances around the pore in question, we obtain a set of voxels that surround the pore but does not include other nearby pores. Fig. 3 shows the output of this algorithm for an Example 2D slice. The red line is the bounding box used to crop the distance transform map while the blue line displays our computed pore neighborhood.

A third feature is the longitudinal aspect ratio. It captures the elongation along the build direction (keyhole) or along the scan direction (lack-of-fusion). The feature is defined as:

$$AR = \frac{Z_{bb}}{\max(\mathbf{D}_{xy})} \tag{3}$$

with Z_{bb} being the pore height as determined by calculating the bounding box. $\max(\mathbf{D}_{xy})$ is again the width of the pore as defined earlier. For keyhole pores, their elongation along the build direction results in a aspect ratio value close to 1. For lack-of-fusion pores, these values are lower due to their elongation within the XY-plane.

Some 3D renderings of example pores can be seen on Fig. 4a (lack-of-fusion) and Fig. 4b (keyhole). Note the more spherical/el-

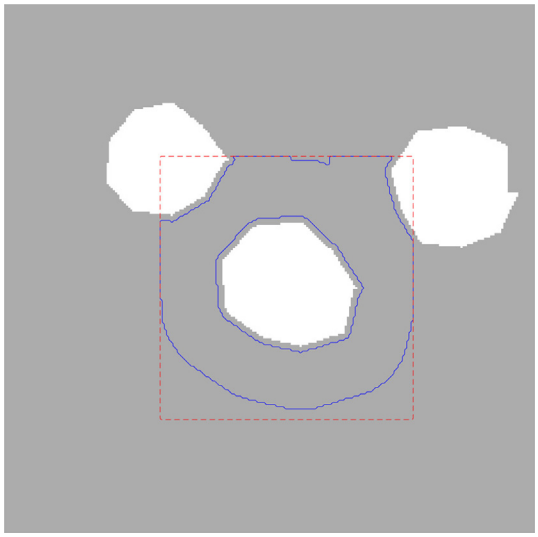

Fig. 3. Result of the described method for determining a pore's neighborhood. The red line being the bounding box, while the blue line is the pore's neighborhood determined by thresholding the distance transform in this bounding box.

lipsoidal structure of the keyhole pores and their height (Z-axis) to width ratio (in the XY-plane) compared to the lack-of-fusion pores.

3.4. Classification

Finally, given the proposed feature values of the pores, a machine learning classifier is trained to classify a pore as either being a keyhole or lack-of-fusion type. This is a binary classification problem with few features, so a simple classifier should suffice. There is likely no need for deep learning, boosting, or highly-elaborate techniques. As a result, a Bayes classifier [66] is leveraged here for pore classification, with an equal prior of 0.5 on both pore type classes. The amount of keyhole pores and lack-of-fusion pores expected in a randomly selected part depends on a lot on the printing conditions, and thus is very hard to determine. For these reasons, an equal prior for both the pore classes is the most suitable approach. The Bayes model also assumes a normal (Gaussian) distribution for the density estimations.

4. Experimental setup

To train and evaluate our classifier, and to evaluate the robustness of our chosen features, multiple test objects were printed with the design shown in Fig. 5. The object consists of a main cylinder with a diameter of 5 mm and height of 17 mm. This cylinder sits on an asymmetrical base plate that is removed when cutting the object off of the build plate. Protruding from the sides of the cylinder are small cylinders of 0.55 mm in diameter angled at 45 degrees. These cylinders are distributed every 90 degrees in the horizontal plane and every 3.3 mm along the vertical axis of the main cylinder. A pattern of small indentations were made in the top 0.6 mm of the main cylinder to identify, and provide a frame of reference for the printed object. This design was printed in 316L stainless steel, cobalt-chrome, and Ti6Al4V titanium.

This design was chosen because it is easy to print and easy to align with CT reconstructions by matching the smaller cylinders. The cylinder is the main part where the porosity will be studied, the square plate forms the interface between the build plate and the main cylinder. The plate is also useful for identification of the first layer of the main test object (the cylinder) and can help in alignment.

The majority of the test object was printed with optimal laser parameters, with the exception of 14 zones within the main cylinder where we aim to induce porosity of known types. A subset of these zones is shown in Fig. 6a. Each zone consists of three consecutive print layers where the middle 25 scan lines are printed with off-nominal laser settings. The laser pattern for one of these layers is shown in Fig. 6b. With the hatching pattern of the print being rotated 67 degrees every layer, the pattern of off-nominal printing for all three layers in the zone looks as shown in Fig. 6c. This pattern creates areas of single-, double-, and triple-layer printing errors, which provides additional variations in printing conditions. In between these porosity-inducing zones, we printed at least 1 mm of nominal layers, thereby avoiding that pores from one section are confused with those from another section.

Table 1 shows the relative energy density, compared to the optimal energy density, and the expected porosity of each of these zones. Zone 0 is used to depict optimal layers where no porosity is expected. The other 14 zones are defect zones created approximately every 30 layers. For every defect zone, the energy density is adjusted by multiplying the optimal energy density by a specific factor. A large range of factors were chosen (0.25 to 4) for two reasons. First, the optimal zones (in the laser parameter space) for these materials vary based on printing conditions. By choosing a large range, we maximize the probability of creating pores in at least some defect zones. Second, the different factors simulate the creation of pores under varying degrees of deviation from the optimal. Note that due to limitations in printer settings, the energy density factors are slightly different for the cobalt-chrome sample and are indicated in parentheses.

The increase or decrease of the energy densities were achieved by fixing all laser parameters to their optimal values and then increasing or decreasing one laser parameter in a way that impacts the emitted energy. For the stainless steel and titanium samples, the laser power was fixed while the laser speed was decreased from zone 1 to 6. From zone 7 to 9 the laser speed was fixed while the laser power was increased. This was done similarly for the cobalt-chrome sample, but since this sample was created with a pulse laser machine, the laser point distance and exposure time were adjusted instead of laser speed.

It is important to note that the energy density alone does not dictate whether pores will be generated. The creation of a pore is a stochastic process and the particular process parameter that was adjusted to reach a specific energy density must also be considered. For example, zone 4 and zone 9 have the same relative energy density of 2.5, but that does not necessarily mean that the amount of keyhole porosity observed in one of these zones is the same as the amount observed in the other. In conclusion, the zones with an equal relative energy density do not represent the same type of deviation from the optimal printing conditions. Therefore, Tables B.1–B.3 in the appendix show the used laser parameters together with the absolute energy density for both samples. For the stainless steel sample, the energy density is calculated by: $E = P/(v\,h\,z)$. where P is the power of the laser, v the speed, h the hatch spacing and z the thickness of the layer. For the cobalt-chrome sample (pulse laser) this equation is instead: $E = P/(v'\,h\,z)$, where $v' = d/t_{on}$ is the ratio of the laser point distance d to the laser exposure time t_{on}. .

Fig. 7a–c show scatter plots of the pore locations of each printed object plotted in the YZ plane. On the right of each figure is a histogram of the pore count binned according to the print layers. On these figures, the green lines indicate the top layer of defect zones that may contain lack-of-fusion pores, while the red lines indicate

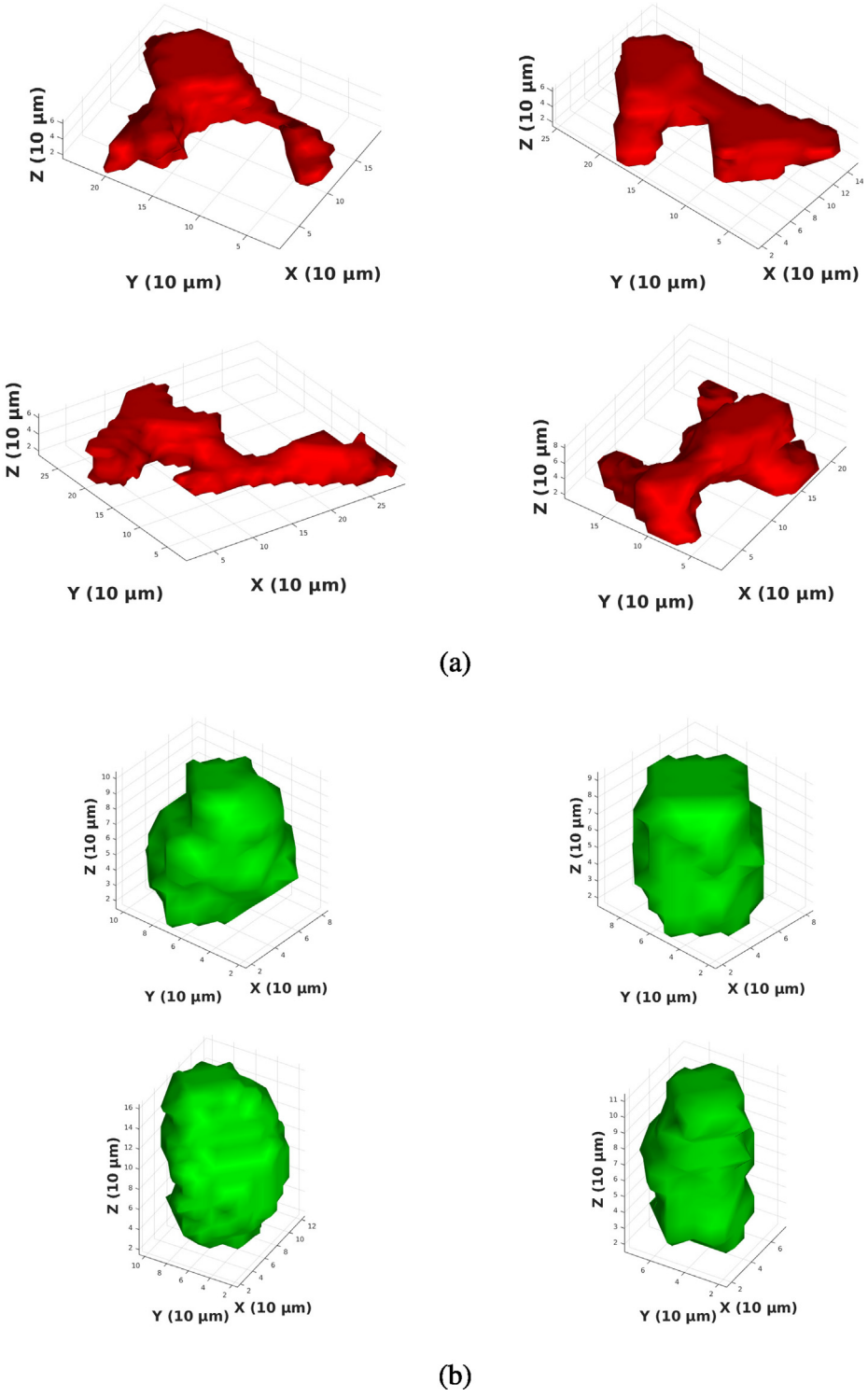

Fig. 4. 3D rendered examples of **(a)** lack-of-fusion pores and **(b)** keyhole pores.

defect zones where keyhole pores are likely to be introduced. The lowest line is zone 1 as described in Table 1.

As expected, not every defect zone generated porosity. However, we can see some clear increases of porosity in certain layers. For stainless steel, Fig. 7a, we can observe an increase of porosity underneath keyhole zones 3 to 6 and an increase of porosity at lack-of-fusion zone 14. In the cobalt-chrome sample, Fig. 7b, there is an increase of porosity underneath keyhole zones 5 and 6, and lack-of-fusion zones 11 and 14. The titanium sample, Fig. 7c, shows an increase in porosity for lack-of-fusion zones 10, 12 and 13. A clear increase can also be observed for keyhole zone 6 and, albeit small, for keyhole zone 4.

In addition to the pores created due to the defect zones, there is an increase of porosity at the side protrusions due to geometry effects, and an increase of porosity near the borders of the samples due to turn-point defects [67]. Note that this is less evident in the YZ-projection but can be seen more clearly on a XY-projection if the pores created by the defect zones are omitted, as illustrated

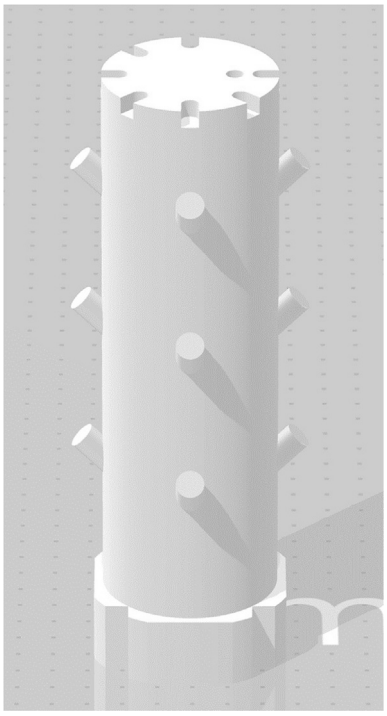

Fig. 5. Visualization of the printed test object.

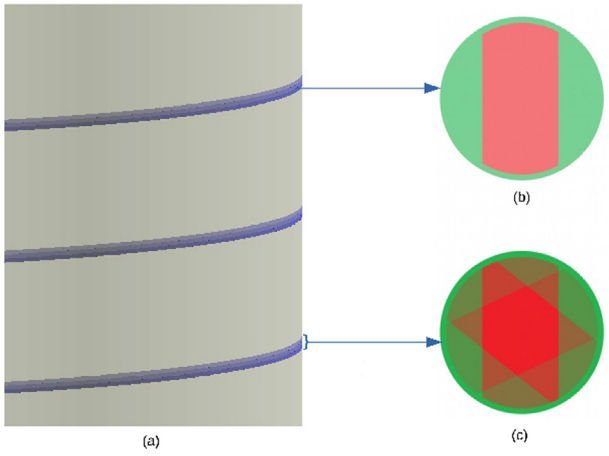

Fig. 6. Pores are induced by using of-nominal laser parameters in zones three layers thick and 1 mm apart. **(a)** a region of the main cylinder showing three pore-inducing zones. **(b)** a layer in the pore-inducing zone; scan lines with off-nominal laser parameters are shown in red. **(c)** an overlay of scan line patterns for the three off-nominal layers in the pore-inducing zone.

on Fig. 8. Although these pores could probably also be attributed to be either keyhole or lack-of-fusion porosity, they were not generated in a controlled way and, therefore, there is uncertainty on their labels. As a result, we do not use these pores near the edges of the object for training or validation.

The keyhole and lack-of-fusion pores generated by the described method were used to create a dataset for supervised classification and feature distribution analysis. However, a specific policy must be defined to formally label these pores. Lack-of-fusion pores are formed on the layer itself, where the parameters are non-optimal [25]. This can also be observed on Fig. 7. Considering this, we make the following assumption: the centroid of lack-of-fusion pores are positioned at the lack-of-fusion defect layers. For example, if a lack-of-fusion defect zone is at layers 200, 201 and 202, all

Table 1
The different defect zones with their relative energy density with respect to the optimal energy density and the expected porosity. Note that some zones were defined slightly differently for the cobalt-chrome and titanium sample, indicated in parenthesis and brackets respectively.

Zone ID	Relative Energy Density	Expected Porosity
0	1	None (fully dense)
1	1.25	Keyhole
2	1.5	Keyhole
3	2	Keyhole
4	2.5	Keyhole
5	3	Keyhole
6	4	Keyhole
7	1.5	Keyhole
8	2	Keyhole
9	2.5 [2]	Keyhole
10	0.75	Lack-of-fusion
11	0.5	Lack-of-fusion
12	0.75 (0.8)	Lack-of-fusion
13	0.5 (0.67)	Lack-of-fusion
14	0.25 (0.50)	Lack-of-fusion

pores within those layers are considered lack-of-fusion pores. Meanwhile, keyhole pores are created below the layer where an increase of energy density is applied [68]. This phenomenon can also be observed on Fig. 7. Here we make the common assumption that they will appear at maximum 20 layers below the keyhole defect layers [25]. Additionally, for both pore types, the inclusion of the pores at the edges and in the side protrusions are avoided by assuming that the pores are created within 2 mm from the center axis of the samples.

For the stainless sample, a total of 3279 pores are labeled as keyhole pores and 50 pores are labeled as lack-of-fusion pores. For the cobalt-chrome sample, we obtained 486 keyhole pores and 214 lack-of-fusion pores. In the titanium sample, 22 keyhole and 346 lack-of-fusion pores were obtained. It is evident that there is a class imbalance, especially for the stainless steel and titanium samples. To deal with this, SMOTE (Synthetic Minority Oversampling Technique) [69] was leveraged to over-sample the minority class. SMOTE creates new samples for a class by interpolating between the feature values of existing samples of that class. When performing the interpolation, the choice of the amount of samples must be carefully considered. If the number is low, the amount of synthetic samples that can be created is low. If the number is high, more samples can be created. However, if we consider potentially very distant neighbors for interpolation, the interpolated features can potentially be considerably altered from what is present in the class. In this work, the 5 nearest neighbors were considered for generating extra samples. For the cobalt-chrome sample, the lack-of-fusion samples were oversampled to 486 to achieve a balanced dataset. For the stainless steel sample, the maximum amount of lack-of-fusion samples that may be synthesized, considering 5 nearest-neighbors is 250 for a total of 300 samples. The keyhole pores were then uniformally downsampled to 300 samples to achieve a balanced dataset. In the titanium sample, the keyhole pores were oversampled to 132, the lack-of-fusion samples were downsampled to the same amount.

For the inner-material classification, training and validation was done using a 5-fold cross-validation. The features were statistically normalized fold-wise by the mean and standard deviation of the training samples. For the cross-material classification, all the samples of one material were considered as the training set, the samples of the others materials were then used as validation set. Again, all features are normalized by the mean and standard deviation of the training samples. Analysis of the feature distributions across laser parameters and across materials was done on the unaltered data, i.e. without SMOTE. All the experiments were conducted using MATLAB version R2020a.

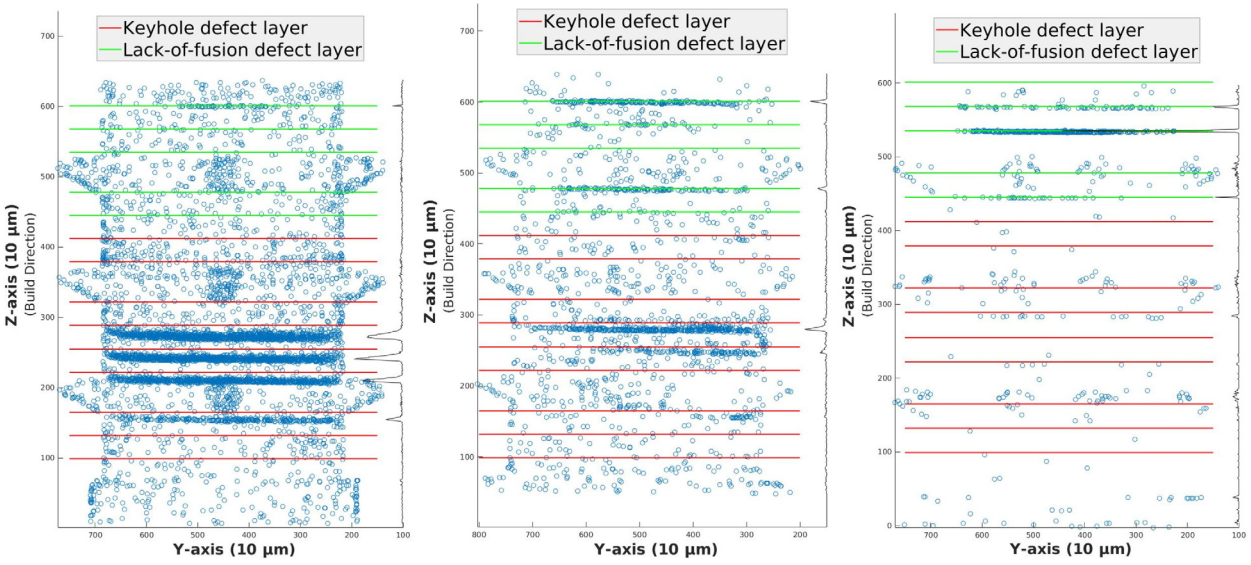

(a) 316L stainless steel (b) Cobalt-chrome (c) Titanium

Fig. 7. Visualization of pore locations in the YZ plane for (**a**) the 316L stainless steel sample, (**b**) the cobalt-chrome sample and (**c**) the titanium sample. The green lines indicate the defect layers where the energy density was lowered, red lines an increased energy density, as described in Table 1. On the right of each figure, histograms of the pore counts per print layer are plotted.

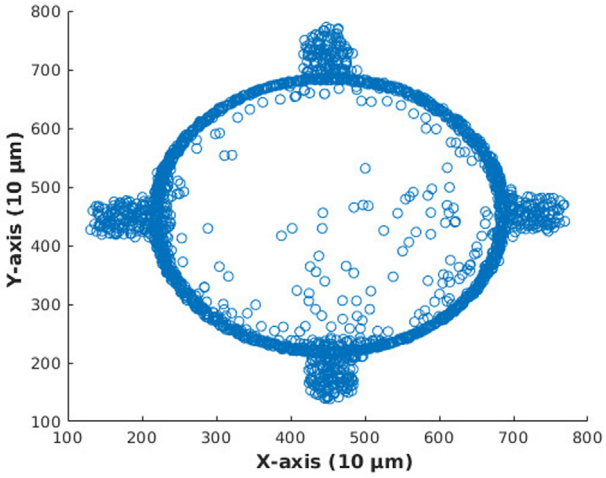

Fig. 8. XY view of the stainless steel sample with the porosity created by the defect zones omitted. The bulk of the pores are situated in the protrusions due to geometry effects and near the border due to turn-point effects.

5. Results

5.1. Robustness to varying printing parameters

The distributions of each feature value for both materials can be seen on Fig. 9, grouped over all defect zones. Because not all defect zones produced porosity, only the relevant zones are shown here. These feature distributions were acquired by calculating a histogram, i.e. grouping the values into bins and normalizing the result according to the total number of values. For the longitudinal aspect ratio and the compactness, the bins have size 0.1, for the relative mean intensity, the size is 0.05, due to the smaller range.

The influence of the laser parameters on the features can be quantified by means of linear regression analysis. For every feature Y, a multiple linear regression model is fitted for both pore types and materials: $Y = w_1X_1 + w_2X_2 + b$, where X_1 and X_2 denote the laser speed and power respectively, while w_1, w_2 and b are the model parameters to be estimated. The prediction errors, or residuals, are used to calculate the coefficient of determination R^2. This coefficient provides a measure of how well the variance in the feature values is explained by the changes in laser parameters. These values can be observed for all three materials in Table 2. In all cases, the R^2 values are less than 0.20, and only one of the values exceeded 0.08. Note that for the lack-of-fusion pores of the steel sample, this analysis was not possible due to there being only a single lack-of-fusion pore creation zone.

It is evident from the figures and the R^2 values that the laser parameters have very little influence on the keyhole distributions. For the stainless steel sample, the most notable outlier is the relative mean intensity of the keyhole pores, with a R^2 value of 0.05100. Fig. 9b (left image) shows that these distributions shift towards the right as the energy density increases. This shift can most likely be attributed to the partial volume effect. As the energy density increases, so will the volume of the keyhole pores. Consequently, the partial voluming effect will have less of an influence on these larger pores, increasing the relative mean intensity. Fortunately, the distributions shift away from the lack-of-fusion distribution, indicating it should not to be troublesome for pore type classification.

For the lack-of-fusion pores in the cobalt-chrome and titanium samples, a larger R^2 is observed for both the aspect ratio and the compactness. The small difference in distributions can be attributed to different pore widths across the laser parameters. Fig. 10a shows the distributions of these pore widths. Notice a clear increase in pore width for the lack-of-fusion zone 14 compared to zone 11 in the cobalt-chrome sample and the increase from zones 10 to 13 in the titanium sample. Due to the smaller pore widths in the lower zones, the denominator in Eq. (3) decreases, and thus increasing the aspect ratio. Similarly, the denominator of Eq. (1) will decrease fast with decreasing pore widths, increasing the compactness values. Both increases for the aspect ratio and compactness can indeed be observed on Fig. 9a and c (middle and right). Nonetheless, the influence of the laser parameters remains small.

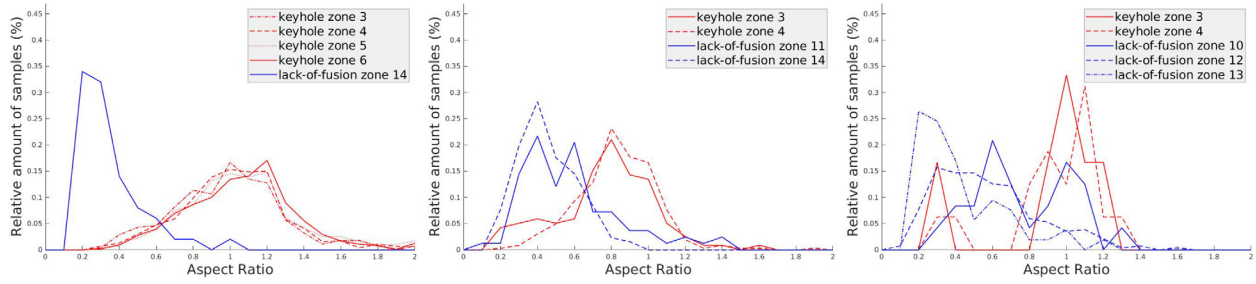

(a) Aspect ratios in stainless steel (left), cobalt-chrome (middle) and titanium (right)

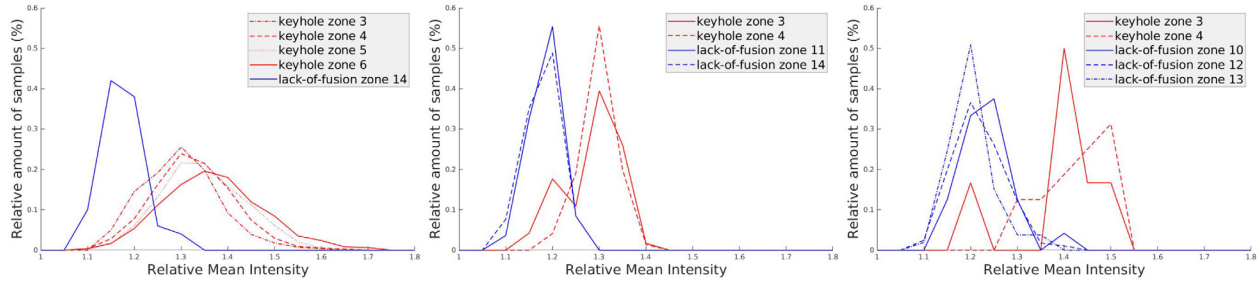

(b) Relative mean intensities in stainless steel (left), cobalt-chrome (middle) and titanium (right)

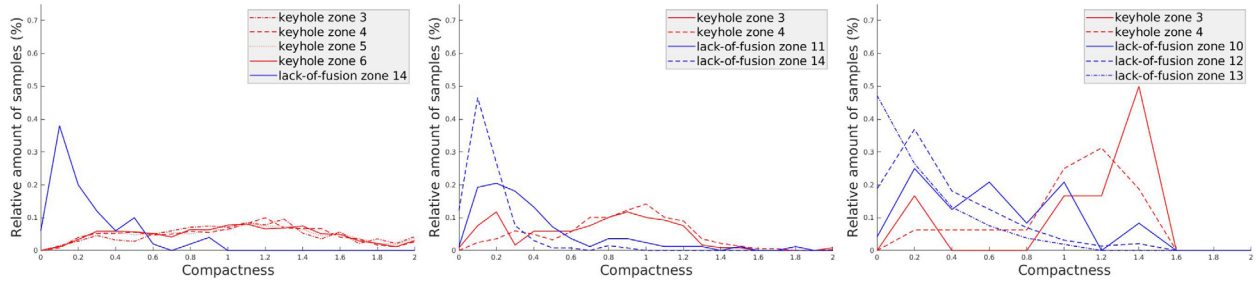

(c) Compactnesses in stainless steel (left), cobalt-chrome (middle) and titanium (right)

Fig. 9. Feature distributions across the different zones as defined in Table 1 for the stainless steel (left), cobalt-chrome (middle) and titanium (right) sample for the **(a)** aspect ratio, **(b)** relative mean intensity and **(c)** compactness.

Table 2
Coefficients of determination as determined by linear regression analysis for the **(a)** stainless steel sample, **(b)** cobalt-chrome sample and **(c)** titanium sample.

Feature	Keyhole R^2	Lack-of-fusion R^2
	(a) 316L stainless steel	
Aspect Ratio	0.00542	–
Relative Mean Intensity	0.05100	–
Compactness	0.00064	–
	(b) Cobalt-chrome	
Aspect Ratio	0.01750	0.09180
Relative Mean Intensity	0.01940	0.00870
Compactness	0.01890	0.19200
	(c) Titanium	
Aspect Ratio	0.00110	0.07580
Relative Mean Intensity	0.01810	0.01950
Compactness	0.01670	0.07750

5.2. Material agnosticism

To confirm that the features are material-agnostic, it is necessary that their distributions do not change considerably across materials. Fig. 11 shows the feature distributions of both materials. Similarly, a linear regression model can be fitted: $Y = w_1X_1 + w_2X_2 + w_3X_3 + b$, where X_1, X_2 and X_3 now denote the three test materials, each as a binary variable. Here, the R^2 values indicate how much of an influence the material type has on the feature values. The values are given in Table 3.

The largest influence of the material type is observed on the aspect ratio and relative mean intensity features. In particular, the aspect ratio values for the cobalt-chrome lack-of-fusion pores have increased while for the keyhole pores, they have decreased, shifting the distributions closer together compared to the steel sample. For the titanium sample, the keyhole aspect ratio distribution seems to overlap better with the steel distribution, albeit with less variance. The lack-of-fusion distribution overlaps better with cobalt-chrome. However, from a classification perspective, an optimal decision boundary to discern between the two classes would be at approximately the same position for all materials, suggesting that these distribution shifts may have limited influence on the classification results. For the relative mean intensity, the steel and cobalt-chrome distribution mostly overlap, the only difference is perhaps a bit more variance on the keyhole distribution of stainless steel. The larger R^2 value for lack-of-fusion can mostly be attributed to the shift of the titanium distribution. This shift causes a slight overlap with keyhole distributions of the other materials, which might have some influence on the cross-material classification.

Meanwhile, there are some less distinctive influences of the material on the compactness distributions. Mainly, it appears that the stainless steel keyhole feature distribution has a larger variance compared to the cobalt-chrome and titanium sample. For the lack-of-fusion, the titanium shows slightly more variance. Again, these changes are minimal and should have very little effect on the classifications results.

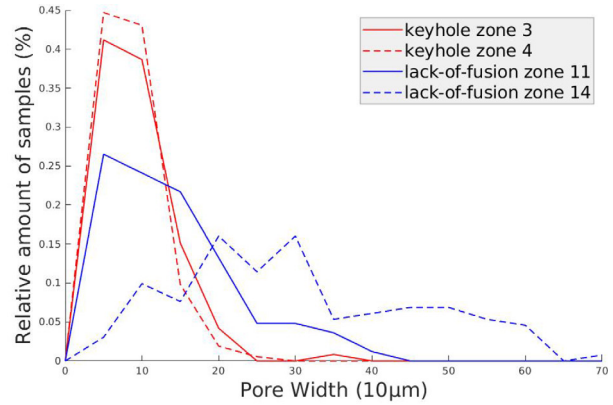

(a) Cobalt-chrome

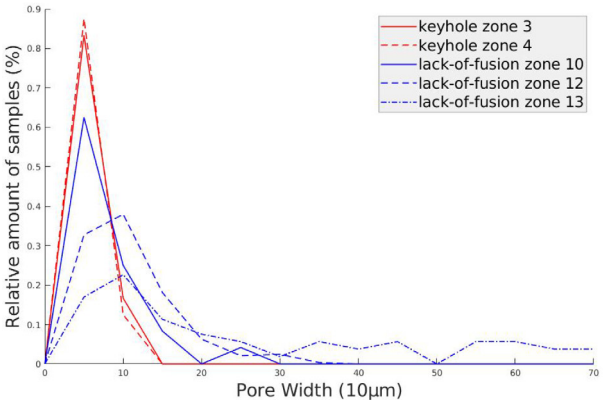

(b) Titanium

Fig. 10. Pore width distributions across the different zones as defined in Table 1 for the **(a)** cobalt-chrome and **(b)** titanium sample.

5.3. Inner-material classification

To show the improved effectiveness of our proposed set of features compared to the state-of-the-art, we compared classification results with our features to the classification results using the features used by Snell et al.: pore sphericity, aspect ratio, and pore length [41]. The work of Snell et al. is the most comparable to our methods as it uses the same type of image data (i.e. X-ray CT) and has the same pore classes as ours.

Table 4 shows quantified classification results between the two feature sets on all three materials (note: lack-of-fusion is abbreviated as l.o.f., keyhole as KH). The shown values have been averaged across the 5 folds and also show the standard deviation. Fig. 12 shows a ROC-curve comparison. The lack-of-fusion is considered to be the positive class here. To compute the ROC-curve across the 5 folds, all the validation outputs were combined.

The table shows a notable improvement on all the performance metrics for both samples. On average, a 9% increase is observed compared to the features as leveraged by Snell et al. For the stainless steel sample, the ROC-curve of our feature set outperforms across the entire range. For the cobalt-chrome and titanium samples, we observed a better performance by the features by Snell et al. for small false positive rates. However, our method comes closer to the theoretical *perfect classifier* (upper left corner).

We believe this improvement is due to three reasons. First, the use of our new pore feature, the relative mean intensity, seems to have a positive impact. From the distribution analysis, it is clear that this feature is informative for the classification between keyhole and lack-of-fusion pores. Additionally, it is robust to laser parameter and material changes. Second, the use of the pore length feature by Snell et al. may have decreased their classification accuracy. Although it has been noted in many studies that keyhole pores tend to be smaller than lack-of-fusion pores, this only seems to be the case for small deviations from the optimal conditions. In our experiments, we observe significant overlap in the keyhole pore length distributions and lack-of-fusion distributions, as seen on Fig. 13. These overlaps were detrimental to the classification.

Third, the compactness feature is more robust to changes in laser parameters than the sphericity feature as used by Snell et al. The R^2 values from the sphericity feature by laser parameter regression were $0.01030, 0.02860, 0.28800, 0.0000$ and 0.18500 for the stainless steel keyhole, cobalt-chrome keyhole, cobalt-chrome lack-of-fusion, titanium keyhole and titanium lack-of-fusion distributions respectively. These results are higher than what we observed with the compactness feature, which had R^2 values of $0.00064, 0.01890, 0.19200, 0.01670$ and 0.07750 respectively.

5.4. Cross-material classification

Finally, we test the feature material agnosticism by cross-material classification. For this, a classification model is trained with pore data of one material and then validated on the pore data of the other materials. If the features satisfy this property, we expect similar performance metrics as seen in the inner-material classification. A comparison of the performance metrics between the cross- and inner-material classification can be seen in Table 5. The ROC-curve comparison can be seen in Fig. 14.

We can observe a small decrease on the performance metrics compared to the inner-material classification for steel and cobalt-chrome when training on the other. For the stainless steel sample, there is an average performance decrease of 2.8% and for the cobalt-chrome sample, 4.5%. The ROC-curves, Fig. 14a and b, tell the same story: a slight decrease that is a bit more noticeable for the cobalt-chrome sample.

The decrease in performance is not unexpected. Even though we have shown the influence of material type to be small, it is not negligible. Consequently, the optimal decision boundaries in the feature space are slightly different across materials, inevitably leading to more misclassifications. However, the drop in accuracy is relatively small. In fact, if we compare our cross-material classification to the inner-material classification results using the features of Snell et al. [41], as seen on Fig. 15a and b, we can conclude that it is still outperforming the inner-material classification with the features of Snell et al.

The cross-material classification results on the titanium sample show a bigger drop in performance. Using titanium as a training set an average performance drop of 14.8% and 16.5% is observed for steel and cobalt-chrome respectively. Using the steel and cobalt-chrome as training set and validating on titanium, a drop of 17.0% is observed for steel and 12.9% for cobalt-chrome. This drop in accuracy can most likely be attributed to the shift of the relative mean intensity feature distribution, as seen of Fig. 11c. This shift causes a significant overlap of the titanium lack-of-fusion distributions with the keyhole distributions of steel and cobalt-chrome, leading to misclassifications.

However, the ROC-curves in Fig. 14 tell a different story: using titanium as training set seems to perform better compared to using cobalt-chrome (Fig. 14a) and steel (Fig. 14b) as training set. Additionally, Fig. 14c shows that there is only a very small degradation in performance. This contrast between what is observed on the tables and the ROC-curves is due to the different approach to selecting the most probable class given the classification output. For each sample, the Naive Bayes classifier outputs a probability

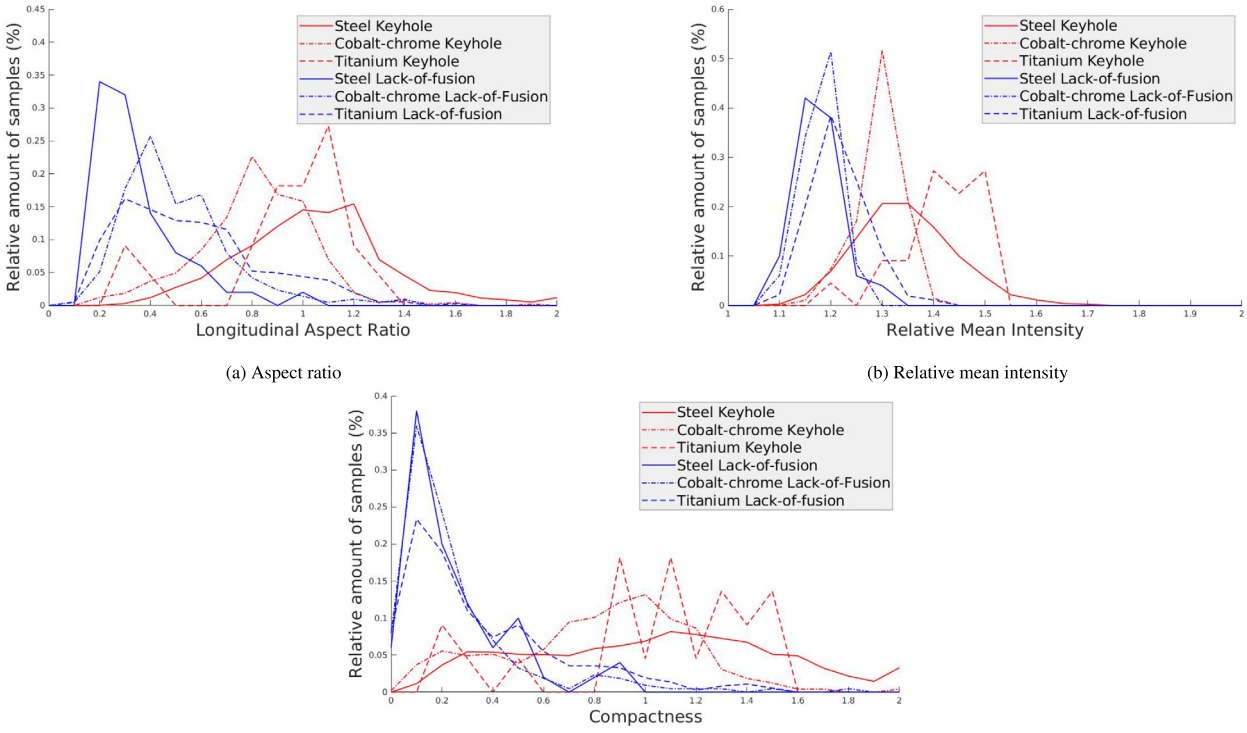

(a) Aspect ratio

(b) Relative mean intensity

(c) Compactness

Fig. 11. Histograms of the keyhole and lack-of-fusion pores for each material of the **(a)** aspect ratio, **(b)** relative mean intensity and **(c)** compactness features.

Table 3
Coefficients of determination as determined by linear regression analysis for the feature distributions across materials.

Feature	Keyhole R^2	Lack-of-fusion R^2
Aspect Ratio	0.06740	0.05510
Relative Mean Intensity	0.03780	0.14360
Compactness	0.02300	0.03090

Table 4
Comparison of the inner-material classification results between our features and the features of Snell et al. [41] for **(a)** the stainless steel sample, **(b)** the cobalt-chrome sampleand **(c)** the titanium sample.

Metric	Ours	Snell et al.
	(a) 316L stainless steel	
Accuracy	$\mathbf{0.930 \pm 0.010}$	0.873 ± 0.027
KH F-score	$\mathbf{0.928 \pm 0.008}$	0.881 ± 0.026
L.o.f. F-score	$\mathbf{0.932 \pm 0.012}$	0.864 ± 0.029
	(b) Cobalt-chrome	
Accuracy	$\mathbf{0.922 \pm 0.032}$	0.839 ± 0.045
KH F-score	$\mathbf{0.917 \pm 0.040}$	0.848 ± 0.052
L.o.f. F-score	$\mathbf{0.925 \pm 0.027}$	0.827 ± 0.039
	(c) Titanium	
Accuracy	$\mathbf{0.912 \pm 0.044}$	0.785 ± 0.046
KH F-score	$\mathbf{0.910 \pm 0.044}$	0.799 ± 0.042
L.o.f. F-score	$\mathbf{0.911 \pm 0.048}$	0.766 ± 0.058

of each class, for example $[0.3, 0.7]$. The easiest approach is to take whatever class has the highest probability as the classification output, 0.7 in this case. This is equivalent to setting a threshold value at 0.5: if the probability for a given class is larger than the threshold, choose it as the output class. This approach was taken for calculating the performance metrics seen in the tables. A ROC-curve, however, sweeps through a range of different threshold values, and calculates the true positive and false positive rate for each of these values. Seeing that the ROC-curves show better results, this implies that for the titanium sample, better threshold values exist than the 0.5 used for reporting the performance metrics in the tables.

Using Titanium as a training set, the classification model is biased towards outputting the lack-of-fusion label with an almost 100% precision, and high output probability scores $> 99.9\%$. Thus setting the label threshold at 0.999 instead of 0.5 gives 91.8% accuracy, a 91.7% keyhole F1 score and a 91.9% lack-of-fusion F1 score for stainless steel. Similarly, accuracies of $91.3\%, 91.1\%$ and 91.4% were achieved for cobalt-chrome. When using stainless steel and cobalt-chrome as training sets, the classification model is biased towards keyhole pores if validating on titanium. A threshold set at 0.999 for keyhole pores produces again much higher performance metrics: $84.5\%, 85.2\%$ and 83.8% for steel, and $89.1\%, 89.3\%$ and 88.9% for cobalt-chrome. These numbers indeed correspond better to what is seen on the ROC-curves, and are similar to what we see for the other materials.

Despite achieving better results by accounting for the bias in the model, it is hard to argue that this can be leveraged in real use cases. In reality, if classifying unseen data and no labeled samples are available, there is no way to know how the model is biased and thus how to adjust the threshold value for better performance. It does however indicate that higher accuracy is achievable, by perhaps designing classification algorithms that better deal with these biases and take uncertainty of prediction into account.

5.5. Kernel density estimation

Our Bayes classifier assumes a normal (Gaussian) distribution for the density estimations. However, the plots of the feature distributions show that some of these distributions are not normal. As such, there is an opportunity to (potentially) improve the results by choosing distributions that better fit the data for the density estimations.

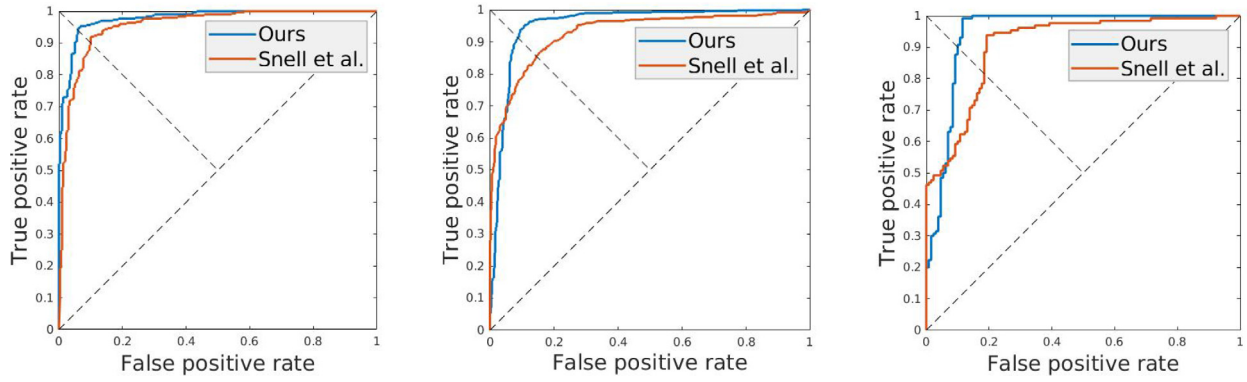

(a) 316L stainless steel (b) Cobalt-chrome (c) Titanium

Fig. 12. ROC curve comparison of the inner-material classification results between our features and the feature of Snell et al. [41] for the **(a)** stainless steel sample, **(b)** cobalt-chrome sample and **(c)** titanium sample.

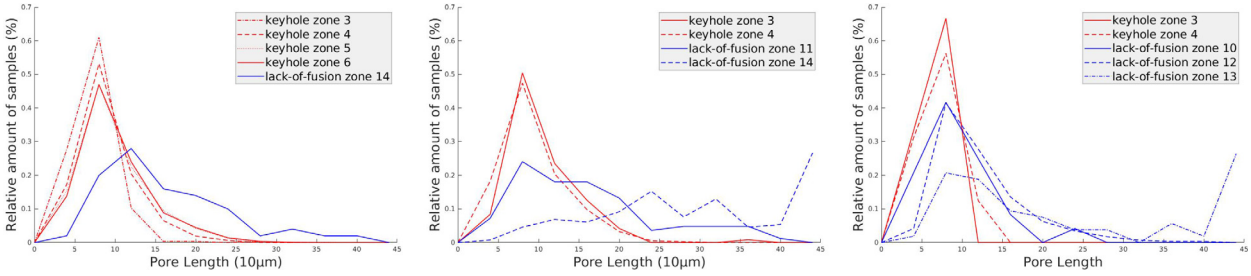

(a) 316L stainless steel (b) Cobalt-chrome (c) Titanium

Fig. 13. Pore length distributions across the different zones as defined in Table 1 for the **(a)** stainless steel sample, **(b)** cobalt-chrome sample and **(c)** titanium sample.

Table 5
Comparison of the cross-material classification compared to the inner-material classification for **(a)** the stainless steel sample, **(b)** the cobalt-chrome sample and **(c)** the titanium sample.

Metric	Training Material		
	(a) 316L stainless steel		
	CoCr	**Ti**	**Steel**
Accuracy	0.902	0.788	0.930 ± 0.010
KH F-score	0.898	0.734	0.928 ± 0.008
L.o.f. F-score	0.906	0.824	0.932 ± 0.012
	(b) Cobalt-chrome		
	Steel	**Ti**	**CoCr**
Accuracy	0.877	0.765	0.922 ± 0.032
KH F-score	0.877	0.695	0.917 ± 0.040
L.o.f. F-score	0.876	0.809	0.925 ± 0.027
	(c) Titanium		
	Steel	**CoCr**	**Ti**
Accuracy	0.745	0.786	0.912 ± 0.044
KH F-score	0.781	0.819	0.910 ± 0.044
L.o.f. F-score	0.696	0.740	0.911 ± 0.048

Table 6 shows a comparison of the inner-material classification results using a Gaussian distribution (previous results) compared to using a kernel density estimator. A kernel density estimator is non-parametric and is able to more closely represent the underlying distributions. It is given by: $\hat{f}_h(x) = \frac{1}{nh}\sum_{i=1}^{n} K\left(\frac{x-x_i}{h}\right)$, where n is the sample size, $K(\cdot)$ the kernel smoothing function, h the bandwidth and $x_1, x_2, \ldots, x_n$ are the samples from the underlying distribution. Here, the kernel smoothing function is a Gaussian. Note that the kernel function determines how much weight is given to neighboring observations, which in this case follows a Gaussian distribution. The resulting density however, is not Gaussian. The bandwidths are calculated for each combination of class and feature by a "rule-of-thumb" formula as formulated in [70] for Gaussian kernels.

A slight improvement is observed for the steel sample, whilst a slight decrease is observed for the cobalt-chrome and Titanium samples. The decrease for cobalt-chrome and titanium can probably be attributed to having more variance in the distributions across laser parameters. However, performing a paired t-test on the performance metrics between the two methods reveals that the changes are not statistically significant for an $\alpha < 0.05$ significance level. Considering this result, it could be argued that it is better to work with the standard Gaussian density estimation, as it is likely to have better generalization. With the kernel density estimation, overfitting could occur due to deviations in the feature distributions.

Table 7 shows the results of performing the same experiment on the cross-material classification, but using kernel density estimation to model the feature distributions. Some small improvement for the stainless steel sample was observed if training on cobalt-chrome but overall it seems that using a Gaussian generalizes better. A paired t-test to test for statistical significance is not possible here, but seeing that a similar outcome is observed as with the inner-material classification, we can probably make the same conclusion.

6. Discussion

The main purpose of this work was to investigate the possibility of a general purpose pore type classifier usable across different print process conditions and printing materials. If such a classifier can be established, pore type information can be learned from pre-

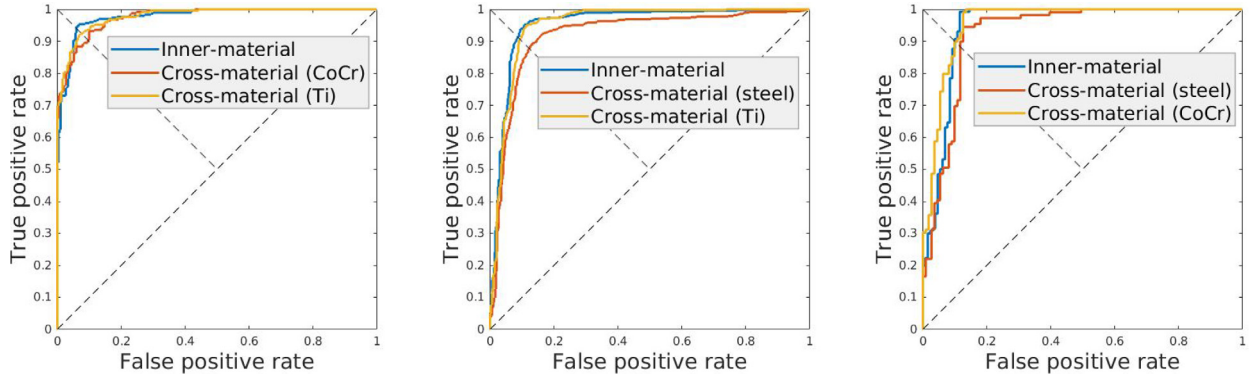

(a) 316L stainless steel (b) Cobalt-chrome (c) Titanium

Fig. 14. ROC curve comparison of the cross-material classification compared to the inner-material classification for the **(a)** stainless steel sample, **(b)** cobalt-chrome sample and **(c)** titanium sample.

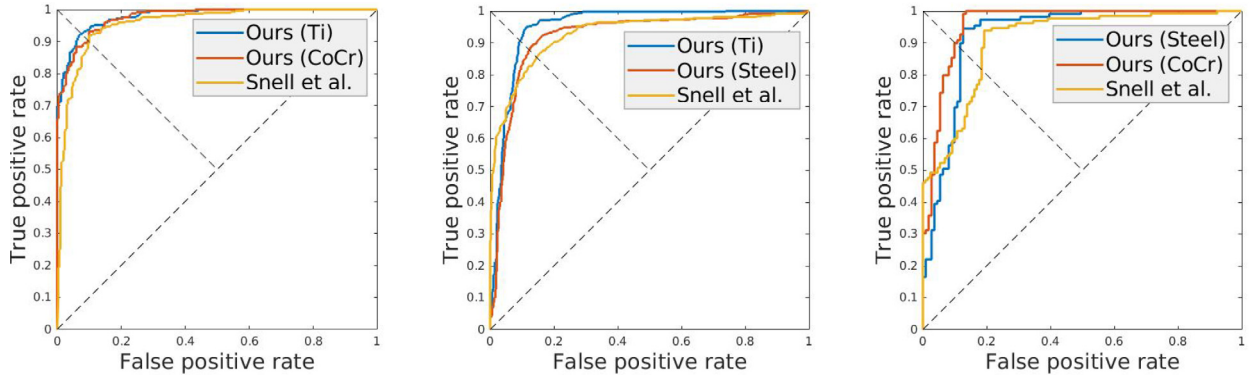

(a) 316L stainless steel (b) Cobalt-chrome (c) Titanium

Fig. 15. ROC curve comparison of our cross-material classification compared to the inner-material classification using the features by Snell et al. [41] for the **(a)** stainless steel sample, **(b)** the cobalt-chrome sample and **(c)** titanium sample.

Table 6
Comparison of the inner-material classification results of using different density estimation techniques for **(a)** the stainless steel sample, **(b)** the cobalt-chrome sample and **(c)** the titanium sample.

Metric	Gaussian	Kernel
	(a) 316L stainless steel	
Accuracy	0.930 ± 0.010	$\mathbf{0.933 \pm 0.013}$
KH F-score	0.928 ± 0.008	$\mathbf{0.932 \pm 0.012}$
L.o.f. F-score	0.932 ± 0.012	$\mathbf{0.934 \pm 0.015}$
	(b) cobalt-chrome	
Accuracy	$\mathbf{0.922 \pm 0.032}$	0.915 ± 0.033
KH F-score	$\mathbf{0.917 \pm 0.040}$	0.911 ± 0.040
L.o.f. F-score	$\mathbf{0.925 \pm 0.027}$	0.918 ± 0.027
	(c) Titanium	
Accuracy	$\mathbf{0.912 \pm 0.044}$	0.896 ± 0.050
KH F-score	$\mathbf{0.910 \pm 0.044}$	0.896 ± 0.046
L.o.f. F-score	$\mathbf{0.911 \pm 0.048}$	0.894 ± 0.060

vious experiments and applied to unseen cases, easing the difficulty of process optimization. We hypothesized that such a classifier is possible and that there must exist some pore features that show minimal variance across materials and process parameters. Our first contribution in this work presents evidence that such features exist. By producing samples in three different materials with porosity introduced using a variety of non-optimal laser parameters, we show that compactness, relative mean intensity, and aspect ratio features are robust to these printing process changes. This result follows from analyzing coefficients of determination (R^2) between the pore features and the laser parameters. The R^2 values are shown to be small, with an average of 0.087, with the largest values attributed to changing pore volumes. Across materials, the average R^2 value was 0.060, with the highest outlier on the relative mean intensity feature, which was attributed to the distribution shift of the titanium sample. This kind of analyses, one that investigates the stability of the chosen features across different printing scenarios, has largely been missing in similar works on pore classification [40–44]. However, we believe it is a necessary step to evaluate the generalisability of a pore type classification method.

For our second contribution, we leveraged our chosen features in a Naive Bayes classifier and evaluated the performance on inner-material classification (i.e. training and validation of pores in single materials) and cross-material classification (i.e. training on pores of one material and validating on another). Accuracies and F-scores of over 90% are achieved for the inner-material classification, which showed 9% improved performance compared to the features used in [41], the most closely related work to ours. Additionally, our results are comparable to other recent works, such as: accuracies above 97% in [43] and a average accuracy of 92.1% in [44]. These numbers demonstrate that state of the art accuracies can be achieved, but with the novelty of doing so under a wider range of printing process conditions, despite the increased variability in pore appearance in these varying conditions, which complicates classification. For the cross-material classification, small

Table 7
Comparison of the cross-material classification results of using different density estimation techniques for **(a)** the stainless steel sample, **(b)** the cobalt-chrome sample and **(c)** the titanium sample.

Metric	CoCr		Titanium	
	Gauss.	Kern.	Gauss.	Kern.
(a) 316L stainless steel				
Accuracy	0.902	**0.906**	**0.788**	0.786
KH F-score	0.898	**0.903**	**0.734**	0.730
L.o.f. F-score	0.906	**0.909**	**0.824**	0.823
	Steel		**Titanium**	
	Gauss.	Kern.	Gauss.	Kern.
(b) Cobalt-chrome				
Accuracy	**0.877**	0.864	**0.765**	0.748
KH F-score	**0.877**	0.866	**0.695**	0.668
L.o.f. F-score	**0.876**	0.862	**0.809**	0.797
	Steel		**CoCr**	
	Gauss.	Kern.	Gauss.	Kern.
(c) Titanium				
Accuracy	**0.745**	0.741	**0.786**	0.759
KH F-score	0.781	**0.782**	**0.819**	0.800
L.o.f. F-score	**0.696**	0.682	**0.740**	0.697

performance drops of 2.8% and 4.5% were observed compared to inner-material classification for the steel and cobalt-chrome samples respectively. This drop is not unexpected, as there were minor distribution shifts across the metals. Nevertheless, the cross-material classification still outperformed the inner-material classification with the features as used in [41]. The drop in performance was higher for the titanium sample but was attributed to the bias in the Naive Bayes model. Adjusting for this bias achieved comparable results. Some studies have investigated pore type classification in multiple materials [41,44], however, they trained different classifiers for each material and validated it only on that same material. To the best of our knowledge, this work is the first to investigate true material agnosticism in pore type classification.

We believe that the reproducibility of the proposed features across the different process conditions and materials can mainly be attributed to the use of only *relative* measurements (e.g. ratios of geometric measurements), as opposed to *absolute* measurements (e.g. pore length, pore volume, etc.) Absolute measurements, albeit informative in some scenarios, are heavily influenced by the physical process of pore creation, which in turn can be altered by material characteristics and process conditions. This became apparent by analysing the pore width and length (Fig. 10a and 13), as it shows that keyhole pores created by high energy densities can easily be as large as lack-of-fusion pores. The low variance of our pore features, together with our high classification performance metrics, indeed support our hypothesis that a general purpose pore type classifier is possible by finding the right features that stay consistent throughout all possible scenarios. This concludes our third and final contribution.

Although we show small variance of feature distributions across materials, we acknowledge that this study only looked at three different types of materials. Future work should include more materials to further investigate the material-agnosticism of the chosen features. On a related note, the same could be said about the robustness to changes in process conditions. As a consequence of not having prior knowledge on the ideal zone of laser parameters for the three materials, some chosen configurations of laser parameters did not provide pores, resulting in only a limited amount of defect zones to study the effect of the laser parameters on the pore features. Future work should look at more configurations of laser parameters that generate porosity for a more conclusive analysis.

Another limitation of this work is the labeling of the pores. We assumed that all pores generated beneath either a keyhole or lack-of-fusion defect zone share that same label. In practice, this might be challenging assumption to validate. There is no guarantee that porosity is not created in the optimally-printed layers. Indeed, we observed a large number of pores at the cylinder contour and side protrusions (Fig. 8). Most of these pores were attributed to geometric and turn-point effects, and we avoided them by only considering pores within a 2 mm radius from the center. Still, there is a possibility of the occasional pore of one type appeared within layers that were considered to only consist pores of a different type. Nevertheless, we suspect that, based on our classification results, the amount of mislabeled pores were likely small enough as not to significantly impact the classification.

The classification of keyhole and lack-of-fusion pores is important because they link to either inserting too much or not enough energy into the powder-bed, respectively. However, these two situations may arise due to a large number of reasons. It could be argued that classification between keyhole and lack-of-fusion pores is not informative enough. After keyhole and lack-of-fusion classification, it might be valuable to further determine the exact cause of the porosity (e.g. powder contamination, build chamber humidity, part geometry). This additional analysis could ease the process of planning a mitigation strategy. Some possible approaches to this additional analysis include relating the pore to its position within the part, or looking into co-occurrence of pores within small regions. The former would identify turn-point effects near the object border, or the need of extra supports for overhanging structures. In the latter case, a large number of nearby pores may suggest environmental problems within the build chamber.

Finally, we acknowledge that this study is not comprehensive. First, as there are still misclassifications, it is obvious that there is room for improvement. Looking at some misclassifications in Fig. 16, it appears that some keyhole pores have a low aspect ratio and do not have this *rounded* structure. On the other hand, for lack-of-fusion pores, it appears that some have a higher aspect ratio and appear to be more rounded. These outliers might arise due to numerous reasons, including the remelting of consecutive layers, pore coalescence, or other types of physical interactions. There might be other types of features that are less dependent on pore morphology that can also deal with these outliers. For example, future work might look at incorporating scan path information. Keyhole pores are known to be formed below a scan path [71], whilst lack-of-fusion pores are formed in between scan paths [72]. Incorporating this information could be valuable, though it is important to note that this extension would require additional processing and, more importantly, requires alignment of the X-ray CT data with the scan path data. Second, it is clear from the analysis on the feature distributions that laser parameters have an influence, albeit small, on some of the features. Most notable, the compactness and aspect ratio change with pore width, and this pore width changes with laser parameters. More thought and work could be put into designing these features to be even more robust. Third, it also evident that the material type has some influence on the feature distributions, most notably on the aspect ratio and relative mean intensity. Future work might involve more materials and analysis to determine what kind of latent variables influence these distributions. If these latent variables can be uncovered, it might be possible to include these variables as features, or at least adjust for them in the feature computations. Lastly, we leveraged a simple classification algorithm in this work. More analysis could be put into finding the optimal classification scheme for this problem. Nevertheless, with this work, we signal a shift towards a more general-purpose approach to the classification of pore types by demonstrating generalization across multiple

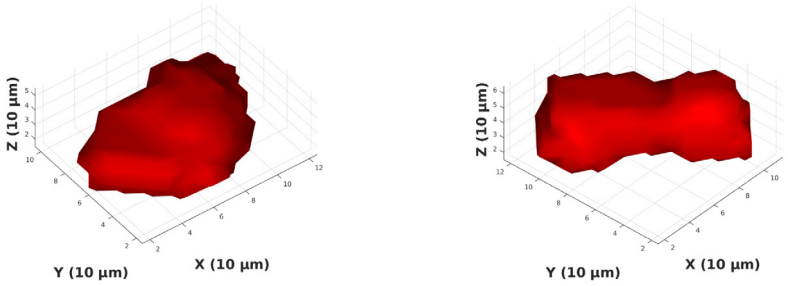

(a) Misclassified keyhole pores

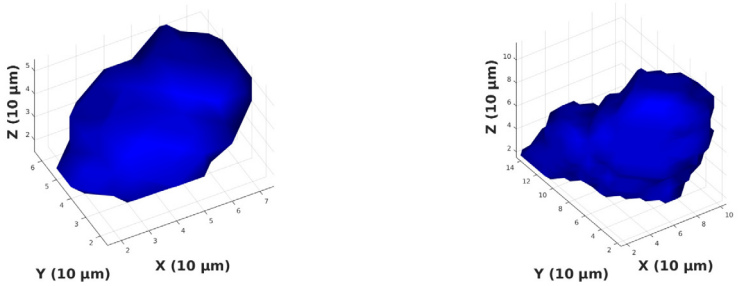

(b) Misclassified lack-of-fusion pores

Fig. 16. 3D rendered examples of misclassifications of **(a)** keyhole pores and **(b)** lack-of-fusion pores.

materials and process conditions whilst still achieving high accuracy.

7. Conclusions

In this work, we proposed the use of material and process agnostic pore features for the classification between keyhole and lack-of-fusion pores, with the intention of creating a general purpose classifier that works across materials and process conditions. We introduced three pore features: the aspect ratio, relative mean intensity, and compactness. We verified the material agnosticism of these features, and their robustness to process conditions, by printing three test samples with known porosities in different materials, then analysing the feature distributions. Second, we trained and validated a classifier for classification of pore types within a single material and across multiple materials (where we trained on pores of a single material and validated on another). The results showed a classification accuracy up to 93.0% of pores within a single material and a accuracy up to 90.2% for the classification across materials, showing that the proposed pore features provide a good basis for a general-purpose pore type classifier.

CRediT authorship contribution statement

Mathieu Vandecasteele: Conceptualization, Methodology, Software, Validation, Formal-analysis, Writing-original-draft, Writing-review-editing. **Rob Heylen:** Investigation, Writing-review-editing. **Domenico Iuso:** Investigation, Writing-review-editing. **Aditi Thanki:** Investigation, Writing-review-editing. **Wilfried Philips:** Supervision, Project-administration, Funding-acquisition, Writing-review-editing. **Ann Witvrouw:** Investigation, Writing-review-editing. **Dries Verhees:** Investigation. **Brian G. Booth:** Conceptualization, Supervision, Project-administration, Writing-review-editing.

Data availability

The data presented in this study are available upon reasonable request from the corresponding author.

Declaration of Competing Interest

The authors declare that they have no known competing financial interests or personal relationships that could have appeared to influence the work reported in this paper.

Acknowledgements

This work was financially supported by the imec ICON VLAIO project ‘Vision in the Loop’ (HBC.2019.2808), a collaboration between TELIN-IPI-imec, Ghent University; Flanders MAKE@KU Leuven; Materialise; imec Vision Lab, University of Antwerp; Flanders MAKE; Dekimo; Manufacturing Processes and Systems (MaPS); ESMA; and AdditiveLab. We wish to thank all the partners for their assistance in technical discussions and data collection.

Appendix A. Microscopy comparison study

The 316L stainless steel sample was first cut into half via EDM wire cutting and then prepared for metallography. The cut-plane was along the build direction. The sample was mounted in resin and later grinding and polishing was performed manually along the cross-section. The metallography was performed to reveal 2D images of porosities using an optical microscopy with a magnification factor of 200. A careful alignment of the metallographic cross-section with the X-CT scan was performed. To match the porosity as seen in the microscopy data with the porosity in the X-ray tomography data, an exhaustive search was done by going through a large range of X-ray slices to visually match pore patterns. An example of such a match is given in Fig. A.1, that shows a good

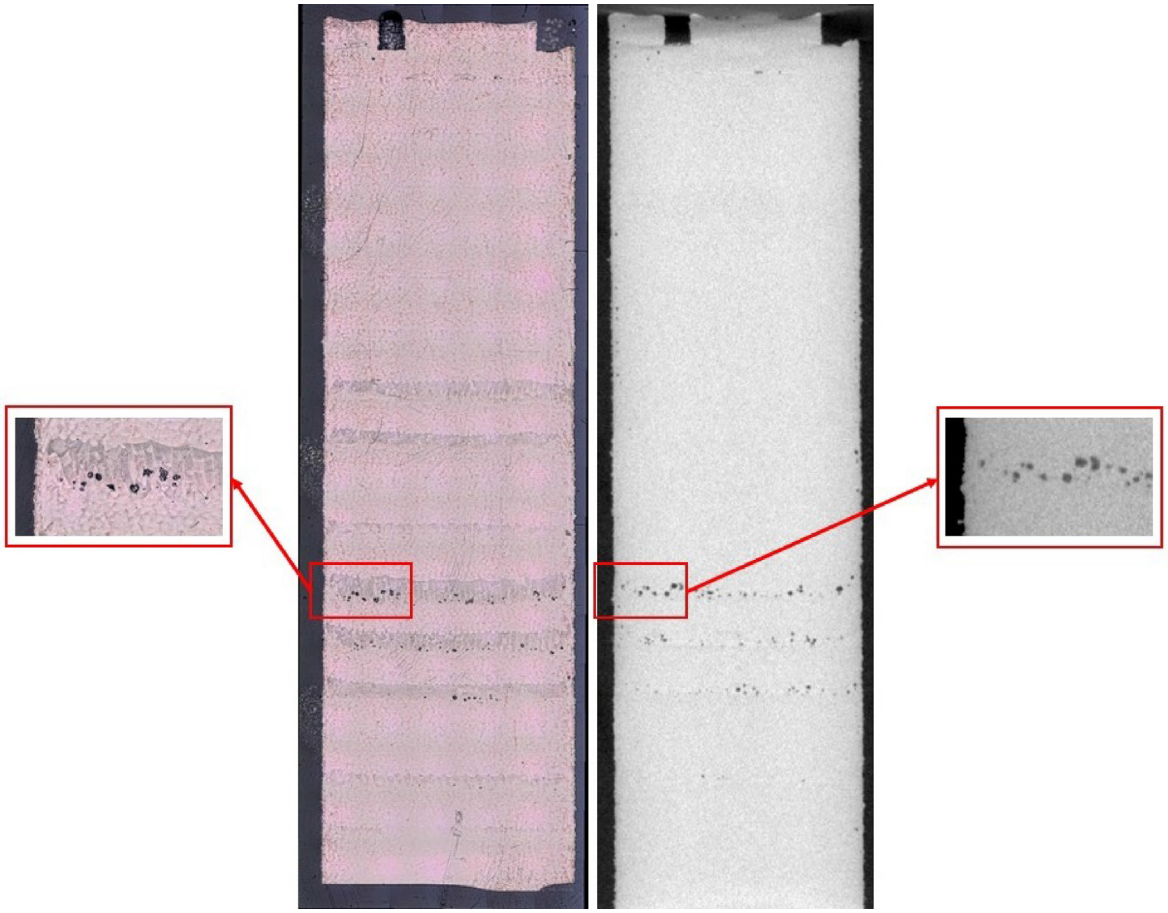

Fig. A.1. An example of a good visual match between the microscopy data (left) and the X-ray tomography data (right) for a group of keyhole pores.

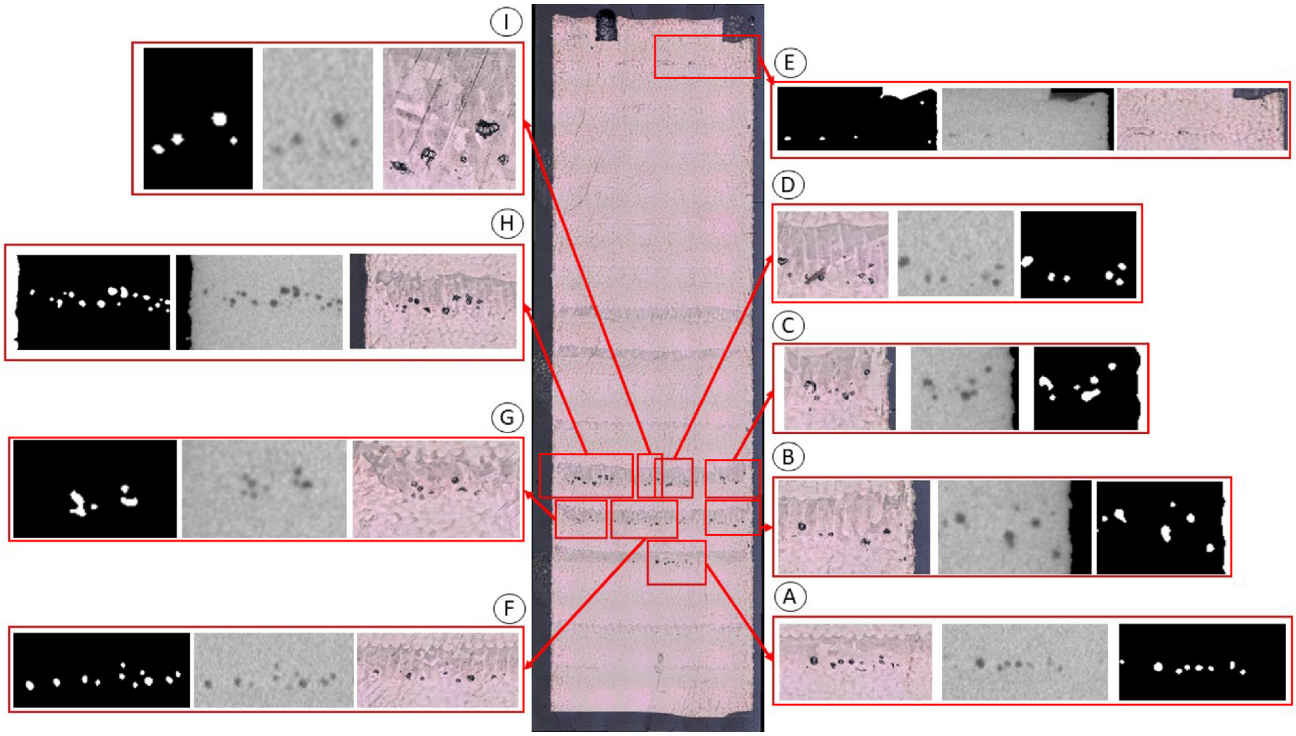

Fig. A.2. Results of the exhaustive search to match pores in the microscopy image with the pores in the X-ray data. For each matching pattern, the binary segmentation, X-ray image and microscopy is shown in more detail. The group of pores labeled E belongs to a lack-of-fusion defect layer. The remaining groups of pores belong to keyhole defect layers.

visual correlation between the microscopy and X-ray for a group of keyhole pores. Fig. A.2 show the results of the exhaustive search for most of the pores that are present in the microscopy data. For each matching pattern, the binary segmentation is also given, as segmented by the technique covered in the Methods section. The group of pores labeled E belongs to a lack-of-fusion defect layer. The remaining groups of pores belong to keyhole defect layers.

Appendix B. Exact laser parameters used in each experiment

Table B.1
Laser parameters used and corresponding energy density and relative energy density (compared to nominal) for each defect zone of the 316L stainless steel sample.

Zone ID	Laser Power (W)	Laser Speed (mm/s)	Energy Density (J/mm^3)	Rel. Energy Density
0	215	900	79.63	1
1	215	720	99.53	1.25
2	215	600	119.44	1.5
3	215	450	159.26	2
4	215	360	199.07	2.5
5	215	300	238.89	3
6	215	225	318.52	4
7	322.5	900	119.44	1.5
8	430	900	159.26	2
9	500	837	199.12	2.5
10	215	1200	59.72	0.75
11	215	1800	39.81	0.5
12	161.25	900	59.72	0.75
13	107.5	900	39.81	0.5
14	53.75	900	19.91	0.25

Table B.2
Laser parameters used and corresponding energy density and relative energy density (compared to nominal) for each defect zone of the 316L cobalt-chrome sample.

Zone ID	Laser Power (W)	Point Distance (μm)	Exposure Time (μs)	Energy Density (J/mm^3)	Rel. Energy Density
0	200	50	55	55.00	1
1	200	50	68.75	68.75	1.25
2	200	50	82.50	82.50	1.5
3	200	50	110	110.00	2
4	200	25	68.75	137.50	2.5
5	200	25	82.50	165.00	3
6	200	25	110	220.00	4
7	200	33.33	55	82.50	1.5
8	200	25	55	110.00	2
9	200	21.50	59.14	137.53	2.5
10	200	50	41.25	41.25	0.75
11	200	50	27.50	27.50	0.5
12	200	62.50	55.00	44.00	0.8
13	200	75	55	36.67	0.66
14	200	100	55	27.50	0.5

Table B.3
Laser parameters used and corresponding energy density and relative energy density (compared to nominal) for each defect zone of the titanium sample.

Zone ID	Laser Power (W)	Laser Speed (mm/s)	Energy Density (J/mm^3)	Rel. Energy Density
0	100	375	68.38	1
1	100	300	85.47	1.25
2	100	250	102.56	1.5
3	100	187.5	136.75	2
4	100	150	170.94	2.5
5	100	125	205.13	3
6	100	93.75	273.50	4
7	150	375	102.56	1.5
8	200	375	136.75	2
9	200	375	136.75	2
10	100	500	51.28	0.75
11	100	750	34.19	0.5
12	75	375	51.28	0.75
13	50	375	34.19	0.5
14	25	375	17.09	0.25

References

[1] M. Javaid, A. Haleem, R.P. Singh, R. Suman, S. Rab, Role of additive manufacturing applications towards environmental sustainability, Adv. Ind. Eng. Polym. Res. 4 (4) (2021) 312–322, https://doi.org/10.1016/j.aiepr.2021.07.005.

[2] M.K. Thompson, G. Moroni, T. Vaneker, G. Fadel, R.I. Campbell, I. Gibson, A. Bernard, J. Schulz, P. Graf, B. Ahuja, F. Martina, Design for Additive Manufacturing: Trends, opportunities, considerations, and constraints, CIRP Ann. 65 (2) (2016) 737–760, https://doi.org/10.1016/j.cirp.2016.05.004.

[3] B. Blakey-Milner, P. Gradl, G. Snedden, M. Brooks, J. Pitot, E. Lopez, M. Leary, F. Berto, A. du Plessis, Metal additive manufacturing in aerospace: A review, Mater. Des. 209 (2021), https://doi.org/10.1016/j.matdes.2021.110008 110008.

[4] A. du Plessis, I. Yadroitsava, I. Yadroitsev, Effects of defects on mechanical properties in metal additive manufacturing: A review focusing on X-ray tomography insights, Mater. Des. 187 (2020), https://doi.org/10.1016/j.matdes.2019.108385 108385.

[5] J.P. Oliveira, A.D. LaLonde, J. Ma, Processing parameters in laser powder bed fusion metal additive manufacturing, Mater. Des. 193 (2020), https://doi.org/10.1016/j.matdes.2020.108762 108762.

[6] L. Englert, S. Czink, S. Dietrich, V. Schulze, How defects depend on geometry and scanning strategy in additively manufactured alsi10mg, J. Mater. Process. Technol. 299 (2022), https://doi.org/10.1016/j.jmatprotec.2021.117331 117331.

[7] Z. Li, H. Li, J. Yin, Y. Li, Z. Nie, X. Li, D. You, K. Guan, W. Duan, L. Cao, D. Wang, L. Ke, Y. Liu, P. Zhao, L. Wang, K. Zhu, Z. Zhang, L. Gao, L. Hao, A Review of Spatter in Laser Powder Bed Fusion Additive Manufacturing: In Situ Detection, Generation, Effects, and Countermeasures, Micromachines 13 (8) (2022) 1366, https://doi.org/10.3390/mi13081366.

[8] D. Ye, K. Zhu, J.Y.H. Fuh, Y. Zhang, H.G. Soon, The investigation of plume and spatter signatures on melted states in selective laser melting, Opt. Laser Technol. 111 (2019) 395–406, https://doi.org/10.1016/j.optlastec.2018.10.019.

[9] A. Mostafaei, C. Zhao, Y. He, S. Reza Ghiaasiaan, B. Shi, S. Shao, N. Shamsaei, Z. Wu, N. Kouraytem, T. Sun, J. Pauza, J.V. Gordon, B. Webler, N.D. Parab, M. Asherloo, Q. Guo, L. Chen, A.D. Rollett, Defects and anomalies in powder bed fusion metal additive manufacturing, Curr. Opin. Solid State Mater. Sci. 26 (2) (2022), https://doi.org/10.1016/j.cossms.2021.100974 100974.

[10] R. Ranjan, C. Ayas, M. Langelaar, F. van Keulen, Fast Detection of Heat Accumulation in Powder Bed Fusion Using Computationally Efficient Thermal Models, Materials 13 (20) (2020) 4576, https://doi.org/10.3390/ma13204576.

[11] J. Tu, I. Miyamoto, T. Inoue, Characterizing keyhole plasma light emission and plasma plume scattering for monitoring 20 kW class CO2 laser welding processes, J. Laser Appl. 14 (3) (2002) 146–153, https://doi.org/10.2351/1.1493763.

[12] D. Joguet, S. Costil, H. Liao, Y. Danlos, Porosity content control of CoCrMo and titanium parts by Taguchi method applied to selective laser melting process parameter, Rapid Prototyp. J. 22 (1) (2016) 20–30, https://doi.org/10.1108/RPJ-09-2013-0092.

[13] Z. Wang, Z. Xiao, Y. Tse, C. Huang, W. Zhang, Optimization of processing parameters and establishment of a relationship between microstructure and mechanical properties of SLM titanium alloy, Opt. Laser Technol. 112 (2019) 159–167, https://doi.org/10.1016/j.optlastec.2018.11.014.

[14] N. Ahmed, I. Barsoum, G. Haidemenopoulos, R.K.A. Al-Rub, Process parameter selection and optimization of laser powder bed fusion for 316L stainless steel: A review, J. Manuf. Process. 75 (2022) 415–434, https://doi.org/10.1016/j.jmapro.2021.12.064.

[15] A. Paraschiv, G. Matache, M.R. Condruz, T.F. Frigioescu, L. Pambaguian, Laser Powder Bed Fusion Process Parameters' Optimization for Fabrication of Dense IN 625, Materials 15 (16) (2022) 5777, https://doi.org/10.3390/ma15165777.

[16] C.L. Druzgalski, A. Ashby, G. Guss, W.E. King, T.T. Roehling, M.J. Matthews, Process optimization of complex geometries using feed forward control for laser powder bed fusion additive manufacturing, Addit. Manuf. 34 (2020), https://doi.org/10.1016/j.addma.2020.101169 101169.

[17] G. Kasperovich, R. Becker, K. Artzt, P. Barriobero-Vila, G. Requena, J. Haubrich, The effect of build direction and geometric optimization in laser powder bed fusion of Inconel 718 structures with internal channels, Mater. Des. 207 (2021), https://doi.org/10.1016/j.matdes.2021.109858 109858.

[18] B.M. Colosimo, S. Cavalli, M. Grasso, A cost model for the economic evaluation of in-situ monitoring tools in metal additive manufacturing, Int. J. Prod. Econ. 223 (2020), https://doi.org/10.1016/j.ijpe.2019.107532 107532.

[19] J. Fiocchi, A. Tuissi, C.A. Biffi, Heat treatment of aluminium alloys produced by laser powder bed fusion: A review, Mater. Des. 204 (2021), https://doi.org/10.1016/j.matdes.2021.109651 109651.

[20] A. Chmielewska, B. Wysocki, P. Kwaśniak, M.J. Kruszewski, B. Michalski, A. Zielińska, B. Adamczyk-Cieślak, A. Krawczyńska, J. Buhagiar, W. Świeszkowski, Heat Treatment of NiTi Alloys Fabricated Using Laser Powder Bed Fusion (LPBF) from Elementally Blended Powders, Materials 15 (9) (2022) 3304, https://doi.org/10.3390/ma15093304.

[21] E. Ghio, E. Cerri, Additive Manufacturing of AlSi10Mg and Ti6Al4V Lightweight Alloys via Laser Powder Bed Fusion: A Review of Heat Treatments Effects, Materials 15 (6) (2022) 2047, https://doi.org/10.3390/ma15062047.

[22] H. Baumgartl, J. Tomas, R. Buettner, M. Merkel, A deep learning-based model for defect detection in laser-powder bed fusion using in-situ thermographic monitoring, Prog. Addit. Manuf. 5 (3) (2020) 277–285, https://doi.org/10.1007/s40964-019-00108-3.

[23] L. Yang, L. Lo, S. Ding, T. Özel, Monitoring and detection of meltpool and spatter regions in laser powder bed fusion of super alloy Inconel 625, Prog. Addit. Manuf. 5 (4) (Dec. 2020), https://doi.org/10.1007/s40964-020-00140-8.

[24] B. Lane, I. Zhirnov, S. Mekhontsev, S. Grantham, R. Ricker, S. Rauniyar, K. Chou, Transient Laser Energy Absorption, Co-axial Melt Pool Monitoring, and Relationship to Melt Pool Morphology, Addit. Manuf. 36 (2020), https://doi.org/10.1016/j.addma.2020.101504 101504.

[25] B.G. Booth, R. Heylen, M. Nourazar, D. Verhees, W. Philips, A. Bey-Temsamani, Encoding Stability into Laser Powder Bed Fusion Monitoring Using Temporal Features and Pore Density Modelling, Sensors 22 (10) (2022) 3740, https://doi.org/10.3390/s22103740.

[26] F. Ahsan, J. Razmi, L. Ladani, Process Parameter Optimization in Metal Laser-Based Powder Bed Fusion Using Image Processing and Statistical Analyses, Metals 12 (1) (2022) 87, https://doi.org/10.3390/met12010087.

[27] N. Diaz Vallejo, C. Lucas, N. Ayers, K. Graydon, H. Hyer, Y. Sohn, Process Optimization and Microstructure Analysis to Understand Laser Powder Bed Fusion of 316L Stainless Steel, Metals 11 (5) (2021) 832, https://doi.org/10.3390/met11050832.

[28] Q. Liu, H. Wu, M.J. Paul, P. He, Z. Peng, B. Gludovatz, J.J. Kruzic, C.H. Wang, X. Li, Machine-learning assisted laser powder bed fusion process optimization for AlSi10Mg: New microstructure description indices and fracture mechanisms, Acta Mater. 201 (2020) 316–328, https://doi.org/10.1016/j.actamat.2020.10.010.

[29] M. Seifi, A. Salem, J. Beuth, O. Harrysson, J.J. Lewandowski, Overview of Materials Qualification Needs for Metal Additive Manufacturing, JOM 68 (3) (2016) 747–764, https://doi.org/10.1007/s11837-015-1810-0.

[30] A.B. Spierings, M. Schneider, R. Eggenberger, Comparison of density measurement techniques for additive manufactured metallic parts, Rapid Prototyp. J. 17 (5) (2011) 380–386, https://doi.org/10.1108/13552541111156504.

[31] A. Sola, A. Nouri, Microstructural porosity in additive manufacturing: The formation and detection of pores in metal parts fabricated by powder bed fusion, J. Adv. Manuf. Process. 1 (3) (2019), https://doi.org/10.1002/amp2.10021 e10021.

[32] J.C. Hastie, M.E. Kartal, L.N. Carter, M.M. Attallah, D.M. Mulvihill, Classifying shape of internal pores within AlSi10Mg alloy manufactured by laser powder bed fusion using 3D X-ray micro computed tomography: Influence of processing parameters and heat treatment, Mater. Charact. 163 (2020), https://doi.org/10.1016/j.matchar.2020.110225 110225.

[33] G. Kasperovich, J. Haubrich, J. Gussone, G. Requena, Correlation between porosity and processing parameters in TiAl6V4 produced by selective laser melting, Mater. Des. 105 (2016) 160–170, https://doi.org/10.1016/j.matdes.2016.05.070.

[34] M. Salarian, H. Asgari, M. Vlasea, Pore space characteristics and corresponding effect on tensile properties of Inconel 625 fabricated via laser powder bed fusion, Mater. Sci. Eng.: A 769 (2020), https://doi.org/10.1016/j.msea.2019.138525 138525.

[35] J.C. Hastie, J. Koelblin, M.E. Kartal, M.M. Attallah, R. Martinez, Evolution of internal pores within AlSi10Mg manufactured by laser powder bed fusion under tension: As-built and heat treated conditions, Mater. Des. 204 (2021), https://doi.org/10.1016/j.matdes.2021.109645 109645.

[36] C. Kim, H. Yin, A. Shmatok, B.C. Prorok, X. Lou, K.H. Matlack, Ultrasonic nondestructive evaluation of laser powder bed fusion 316L stainless steel, Addit. Manuf. 38 (2021), https://doi.org/10.1016/j.addma.2020.101800 101800.

[37] C. Guo, S. Li, S. Shi, X. Li, X. Hu, Q. Zhu, R.M. Ward, Effect of processing parameters on surface roughness, porosity and cracking of as-built IN738LC parts fabricated by laser powder bed fusion, J. Mater. Process. Technol. 285 (2020), https://doi.org/10.1016/j.jmatprotec.2020.116788 116788.

[38] N. Sanaei, A. Fatemi, N. Phan, Defect characteristics and analysis of their variability in metal L-PBF additive manufacturing, Mater. Des. 182 (2019), https://doi.org/10.1016/j.matdes.2019.108091 108091.

[39] W. Liu, C. Chen, S. Shuai, R. Zhao, L. Liu, X. Wang, T. Hu, W. Xuan, C. Li, J. Yu, J. Wang, Z. Ren, Study of pore defect and mechanical properties in selective laser melted Ti6Al4V alloy based on X-ray computed tomography, Mater. Sci. Eng.: A 797 (2020), https://doi.org/10.1016/j.msea.2020.139981 139981.

[40] N. Ellendt, F. Fabricius, A. Toenjes, PoreAnalyzer—An Open-Source Framework for the Analysis and Classification of Defects in Additive Manufacturing, Appl. Sci. 11 (13) (2021) 6086, https://doi.org/10.3390/app11136086.

[41] R. Snell, S. Tammas-Williams, L. Chechik, A. Lyle, E. Hernández-Nava, C. Boig, G. Panoutsos, I. Todd, Methods for Rapid Pore Classification in Metal Additive Manufacturing, JOM 72 (1) (2020) 101–109, https://doi.org/10.1007/s11837-019-03761-9.

[42] N. Nudelis, P. Mayr, A Novel Classification Method for Pores in Laser Powder Bed Fusion, Metals 11 (12) (2021) 1912, https://doi.org/10.3390/met11121912.

[43] A. Poudel, M.S. Yasin, J. Ye, J. Liu, A. Vinel, S. Shao, N. Shamsaei, Feature-based volumetric defect classification in metal additive manufacturing, Nat. Commun. 13 (1) (2022) 6369, https://doi.org/10.1038/s41467-022-34122-x.

[44] W. Cui, Y. Zhang, X. Zhang, L. Li, F. Liou, Metal Additive Manufacturing Parts Inspection Using Convolutional Neural Network, Appl. Sci. 10 (2) (2020) 545, https://doi.org/10.3390/app10020545.

[45] L. Wang, Y. Zhang, H.Y. Chia, W. Yan, Mechanism of keyhole pore formation in metal additive manufacturing, npj Comput. Mater. 8 (1) (2022) 1–11, https://doi.org/10.1038/s41524-022-00699-6.
[46] G. Vastola, Q.X. Pei, Y.W. Zhang, Predictive model for porosity in powder-bed fusion additive manufacturing at high beam energy regime, Addit. Manuf. 22 (2018) 817–822, https://doi.org/10.1016/j.addma.2018.05.042.
[47] W. Wang, J. Ning, S.Y. Liang, Analytical prediction of keyhole porosity in laser powder bed fusion, Int. J. Adv. Manuf. Technol. 119 (11) (2022) 6995–7002, https://doi.org/10.1007/s00170-021-08276-9.
[48] B. Zhang, Y. Li, Q. Bai, Defect Formation Mechanisms in Selective Laser Melting: A Review, Chin. J. Mech. Eng. 30 (3) (2017) 515–527, https://doi.org/10.1007/s10033-017-0121-5.
[49] S.A. Khairallah, A.T. Anderson, A. Rubenchik, W.E. King, Laser powder-bed fusion additive manufacturing: Physics of complex melt flow and formation mechanisms of pores, spatter, and denudation zones, Acta Mater. 108 (2016) 36–45, https://doi.org/10.1016/j.actamat.2016.02.014.
[50] M. Tang, P.C. Pistorius, J.L. Beuth, Prediction of lack-of-fusion porosity for powder bed fusion, Addit. Manuf. 14 (2017) 39–48, https://doi.org/10.1016/j.addma.2016.12.001.
[51] B.D. Samber, J. Renders, T. Elberfeld, Y. Maris, J. Sanctorum, N. Six, Z. Liang, J.D. Beenhouwer, J. Sijbers, FleXCT: a flexible X-ray CT scanner with 10 degrees of freedom, Opt. Express 29 (3) (2021) 3438–3457, https://doi.org/10.1364/OE.409982.
[52] F. Kim, S. Moylan, E. Garboczi, J. Slotwinski, Investigation of pore structure in cobalt chrome additively manufactured parts using X-ray computed tomography and three-dimensional image analysis, Addit. Manuf. 17 (2017), https://doi.org/10.1016/j.addma.2017.06.011.
[53] H. Yeung, F.H. Kim, M.A. Donmez, J. Neira, Keyhole pores reduction in laser powder bed fusion additive manufacturing of nickel alloy 625, Int. J. Mach. Tools Manuf. 183 (2022), https://doi.org/10.1016/j.ijmachtools.2022.103957 103957.
[54] E. Maleki, S. Bagherifard, O. Unal, F. Sabouri, M. Bandini, M. Guagliano, Effects of different mechanical and chemical surface post-treatments on mechanical and surface properties of as-built laser powder bed fusion AlSi10Mg, Surf. Coat. Technol. 439 (2022), https://doi.org/10.1016/j.surfcoat.2022.128391 128391.
[55] E. Maleki, S. Bagherifard, O. Unal, M. Bandini, M. Guagliano, The effects of microstructural and chemical surface gradients on fatigue performance of laser powder bed fusion AlSi10Mg, Mater. Sci. Eng.: A 840 (2022), https://doi.org/10.1016/j.msea.2022.142962 142962.
[56] F.H. Kim, A. Pintar, A.-F. Obaton, J. Fox, J. Tarr, A. Donmez, Merging experiments and computer simulations in X-ray Computed Tomography probability of detection analysis of additive manufacturing flaws, NDT E Int. 119 (2021), https://doi.org/10.1016/j.ndteint.2021.102416 102416.
[57] F.H. Kim, S.P. Moylan, T.Q. Phan, E.J. Garboczi, Investigation of the Effect of Artificial Internal Defects on the Tensile Behavior of Laser Powder Bed Fusion 17–4 Stainless Steel Samples: Simultaneous Tensile Testing and X-Ray Computed Tomography, Exp. Mech. 60 (7) (2020) 987–1004, https://doi.org/10.1007/s11340-020-00604-6.
[58] T.Q. Phan, F.H. Kim, D.C. Pagan, Micromechanical response quantification using high-energy X-rays during phase transformations in additively manufactured 17–4 stainless steel, Mater. Sci. Eng.: A 759 (2019) 565–573, https://doi.org/10.1016/j.msea.2019.05.017.
[59] J. Bernsen, Dynamic thresholding of gray-level images, in: Proceedings - International Conference on Pattern Recognition, Jan. 1986.
[60] A. Rosenfeld, J.L. Pfaltz, Sequential Operations in Digital Picture Processing, J. ACM 13 (4) (1966) 471–494, https://doi.org/10.1145/321356.321357.
[61] S. Beucher, F. Meyer, The Morphological Approach to Segmentation: The Watershed Transformation, in: Mathematical Morphology in Image Processing, vol. 34, 1993, pp. 433–481. doi:10.1201/9781482277234-12.
[62] M. Bayat, A. Thanki, S. Mohanty, A. Witvrouw, S. Yang, J. Thorborg, N.S. Tiedje, J.H. Hattel, Keyhole-induced porosities in Laser-based Powder Bed Fusion (L-PBF) of Ti6Al4V: High-fidelity modelling and experimental validation, Addit. Manuf. 30 (2019), https://doi.org/10.1016/j.addma.2019.100835 100835.
[63] A.A. Martin, N.P. Calta, J.A. Hammons, S.A. Khairallah, M.H. Nielsen, R.M. Shuttlesworth, N. Sinclair, M.J. Matthews, J.R. Jeffries, T.M. Willey, J.R.I. Lee, Ultrafast dynamics of laser-metal interactions in additive manufacturing alloys captured by in situ X-ray imaging, Mater. Today Adv. 1 (2019), https://doi.org/10.1016/j.mtadv.2019.01.001 100002.
[64] M.R. Kabir, H. Richter, Modeling of Processing-Induced Pore Morphology in an Additively-Manufactured Ti-6Al-4V Alloy, Materials 10 (2) (2017) 145, https://doi.org/10.3390/ma10020145.
[65] M. Laleh, A.E. Hughes, S. Yang, J. Wang, J. Li, A.M. Glenn, W. Xu, M.Y. Tan, A critical insight into lack-of-fusion pore structures in additively manufactured stainless steel, Addit. Manuf. 38 (2021), https://doi.org/10.1016/j.addma.2020.101762 101762.
[66] D.J. Hand, K. Yu, Idiot's Bayes: Not So Stupid after All?, Int Stat. Rev./ Revue Internationale de Statistique 69 (3) (2001) 385–398, https://doi.org/10.2307/1403452.
[67] A.A. Martin, N.P. Calta, S.A. Khairallah, J. Wang, P.J. Depond, A.Y. Fong, V. Thampy, G.M. Guss, A.M. Kiss, K.H. Stone, C.J. Tassone, J. Nelson Weker, M.F. Toney, T. van Buuren, M.J. Matthews, Dynamics of pore formation during laser powder bed fusion additive manufacturing, Nat. Commun. 10 (1) (Apr. 2019), https://doi.org/10.1038/s41467-019-10009-2.
[68] A. Thanki, L. Goossens, R. Mertens, G. Probst, W. Dewulf, A. Witvrouw, S. Yang, Study of keyhole-porosities in selective laser melting using X-ray computed tomography, in: 9th Conference on Industrial Computed Tomography (iCT), Jan. 2019. doi:10.29007/3qvj.
[69] N.V. Chawla, K.W. Bowyer, L.O. Hall, W.P. Kegelmeyer, SMOTE: Synthetic Minority Over-sampling Technique, J. Artif. Intell. Res. 16 (2002) 321–357, https://doi.org/10.1613/jair.953.
[70] B.W. Silverman, Density Estimation for Statistics and Data Analysis, London, 1986.
[71] W.E. King, H.D. Barth, V.M. Castillo, G.F. Gallegos, J.W. Gibbs, D.E. Hahn, C. Kamath, A.M. Rubenchik, Observation of keyhole-mode laser melting in laser powder-bed fusion additive manufacturing, J. Mater. Process. Technol. 214 (12) (2014) 2915–2925, https://doi.org/10.1016/j.jmatprotec.2014.06.005.
[72] A. du Plessis, Effects of process parameters on porosity in laser powder bed fusion revealed by X-ray tomography, Add. Manuf. 30 (2019), https://doi.org/10.1016/j.addma.2019.100871 100871.